

THE MASSIVE SURVEY XVI. THE STELLAR INITIAL MASS FUNCTION IN THE CENTER OF MASSIVE EARLY-TYPE GALAXIES

MENG GU¹, JENNY GREENE¹, ANDREW B. NEWMAN², CHRISTINA KREISCH¹, MATTHEW QUENNEVILLE³, CHUNG-PEI MA³ AND JOHN P. BLAKESLEE⁴

Submitted to ApJ

ABSTRACT

The stellar initial mass function (IMF) is a fundamental property in the measurement of stellar masses and galaxy star formation histories. In this work we focus on the most massive galaxies in the nearby universe $\log(M_*/M_\odot) > 11.2$. We obtain high quality Magellan/LDSS-3 long slit spectroscopy with a wide wavelength coverage of $0.4\mu\text{m} - 1.01\mu\text{m}$ for 41 early-type galaxies (ETGs) in the MASSIVE survey, and derive high S/N spectra within an aperture of $R_e/8$. Using detailed stellar synthesis models, we constrain the elemental abundances and stellar IMF of each galaxy through full spectral modeling. All the ETGs in our sample have an IMF that is steeper than a Milky Way (Kroupa) IMF. The best-fit IMF mismatch parameter, $\alpha_{\text{IMF}} = (M/L)/(M/L)_{\text{MW}}$, ranges from 1.12 to 3.05, with an average of $\langle \alpha_{\text{IMF}} \rangle = 1.84$, suggesting that on average, the IMF is more bottom-heavy than Salpeter. Comparing the estimated stellar mass with the dynamical mass, we find that most galaxies have stellar masses smaller than their dynamical masses within the 1σ uncertainty. We complement our sample with lower-mass galaxies from the literature, and confirm that $\log(\alpha_{\text{IMF}})$ is positively correlated with $\log(\sigma)$, $\log(M_*)$, and $\log(M_{\text{dyn}})$. The IMF in the centers of more massive ETGs is more bottom-heavy. In addition, we find that $\log(\alpha_{\text{IMF}})$ is positively correlated with both $[\text{Mg}/\text{Fe}]$ and the estimated total metallicity $[Z/H]$. We find suggestive evidence that the effective stellar surface density Σ_{Kroupa} might be responsible for the variation of α_{IMF} . We conclude that σ , $[\text{Mg}/\text{Fe}]$ and $[Z/H]$ are the primary drivers of the global stellar IMF variation.

Subject headings: galaxies: general — galaxies: stellar content — galaxies: formation — galaxies: evolution — stars: mass function

1. INTRODUCTION

The stellar initial mass function (IMF) describes the distribution of stellar masses at birth in one star formation event, and is a crucial element in astrophysical studies on multiple scales, from the formation of planetary systems to star formation and stellar feedback, from galaxy evolution to the dark matter content. However, constraining the IMF is not easy since it is not directly measurable (Kroupa et al. 2013). Over the past few decades, studies of Galactic field stars and stellar clusters reveal that the stellar IMF within the Milky Way (MW) has little variation and is usually described as the canonical IMF (Scalo 1986; Kroupa 2001; Bastian et al. 2010). The universal canonical IMF is often adopted as a basic assumption in galaxy modeling and interpretation of observational galaxy properties.

The idea of a universal IMF has been challenged by many studies. For early type galaxies (ETGs), this topic have been explored by several independent methods (Smith 2020), including stellar dynamical modeling (e.g. Schwarzschild 1979; Thomas et al. 2011; Dutton et al. 2012; Cappellari et al. 2013a; Li et al. 2017; Liepold et al. 2020; McConnell et al. 2012), strong gravitational lensing (e.g. Spiniello et al. 2011; Treu 2010; Newman et al. 2017), and stellar population synthesis (SPS) (e.g. Cenarro et al. 2003; van Dokkum et al. 2010; van Dokkum et al. 2012; Conroy & van Dokkum 2012b; Villaume et al. 2017; Conroy et al. 2017). In par-

ticular, the SPS method relies on the strength of absorption features in the optical to near-infrared (NIR) that are sensitive to surface gravity (Wing & Ford 1969), as they contain information on the relative fraction of giant and dwarf stars. Current SPS models make use of empirical stellar libraries and theoretical response functions to disentangle various chemical abundances from the stellar IMF (Cenarro et al. 2003; Vazdekis et al. 2016) and constrain the IMF in the low-mass regime ($\leq 1M_\odot$). Usually two approaches are adopted in SPS: the full spectral modeling technique (e.g. Conroy & van Dokkum 2012b; Conroy et al. 2017) or spectral indices analysis (e.g. La Barbera et al. 2019; Martín-Navarro et al. 2021).

SPS studies (e.g. Spiniello et al. 2012; Ferreras et al. 2013; Conroy & van Dokkum 2012b), gravitational lensing studies (e.g. Treu 2010) and dynamical modeling (e.g. Lasker et al. 2013; Cappellari et al. 2013a) all reveal the trend that the IMF becomes increasingly bottom heavy with increasing velocity dispersion in ETGs. The agreement across different methods provides confirmation that the general trend of IMF variation is correct. On the other hand, on an object-by-object basis, the consistency is not necessarily as strong as expected, as shown in Smith (e.g. 2014); Newman et al. (e.g. 2017).

Many studies in recent years have explored possible physical mechanisms behind IMF variation. In addition to the correlation between the IMF and galaxy stellar velocity dispersion, galaxy properties such as mass density (e.g. Spiniello et al. 2015), and stellar populations such as stellar metallicity (e.g. Martín-Navarro et al. 2015; van Dokkum et al. 2017; Parikh et al. 2018), $[\text{Mg}/\text{Fe}]$ (e.g. Conroy & van Dokkum 2012a; Smith et al. 2012), and age (e.g. Barbosa et al. 2021) have been suggested to be correlated with IMF variation. There is still ongoing debate about which galaxy properties

¹ Department of Astrophysical Sciences, Princeton University, Princeton, NJ, USA

² The Observatories of the Carnegie Institution for Science, Pasadena, CA, USA

³ Department of Astronomy and Department of Physics, University of California at Berkeley, Berkeley, CA, USA

⁴ Gemini Observatory and NSF's NOIRLab, 950 N. Cherry Avenue, Tucson, AZ 85719, USA

or physical mechanism is the primary driver of IMF variation.

In this work, we perform a detailed full spectral modeling analysis of the most massive galaxies in the nearby universe to determine their stellar population parameters and stellar IMF. We apply a state-of-the-art stellar synthesis modeling tool to high quality Magellan/LDSS3 optical-NIR spectra.⁵ The sample is selected from the volume-limited MASSIVE survey ($D < 108$ Mpc, $\log(M_*/\odot) > 11.5$). We focus on a narrow mass and velocity dispersion range, and look for correlations between galaxy stellar populations, dynamical properties and the stellar IMF. The goal of this paper is to investigate their central properties (within one eighth of the effective radius R_e). In particular, we combine our sample with lower-mass galaxies from Conroy & van Dokkum (2012a) and Cappellari et al. (2013a), and present the global scaling relations between the IMF and velocity dispersion (σ), stellar mass, and dynamical mass. We examine the relation between the IMF and other galaxy properties in order to find the physical properties responsible for the scatter at fixed velocity dispersion. Furthermore, we test the consistency between our results and dynamical constraints.

In § 2 we summarize the MASSIVE sample, the comparison samples, the observations, and the data reduction procedures. In § 3 we summarize the spectral modeling tool. In § 4 we present our main results, including the central stellar population properties, global scaling relations, and the drivers of IMF variations among galaxies. In § 5 we assess the consistency between the derived stellar IMF and dynamical constraints. We discuss results from different models and the physical implications of our results in § 6.

2. DATA

2.1. Sample

Targets in this work are selected from the MASSIVE survey (Ma et al. 2014). This is a volume-limited sample of the 116 most massive galaxies within 108 Mpc. The survey is already equipped with spatially resolved stellar kinematics from the Mitchell/VIRUS-P Integral Field Spectrograph (IFS) at the McDonald Observatory in 3650–5850Å (Veale et al. 2017b,a; Veale et al. 2018), V and K -band photometry from 2MASS (absolute K -band magnitude $M_K < -25.3$ mag) and wide-field and deep K -band photometry from CFHT. Galaxies in the sample reside in a wide range of environments (Veale et al. 2017a) from isolated to massive galaxy clusters. Therefore the MASSIVE survey contains the ideal sample for a comprehensive study of very high mass galaxies. In this work, we observe 41 ETGs in the MASSIVE survey using the LDSS3, selected based on their declination. These observations significantly extend the S/N and wavelength coverage of the existing spectroscopy.

2.2. Comparison Samples

The goal of the paper is to study the stellar initial mass function within and among massive ETGs. We focus on a relatively narrow range of stellar mass and σ and aim to look for IMF variations with galaxy properties. Another main goal is to study the scatter in the IMF in galaxies with similar σ . To study any global trends involving the IMF, we must also compare our results with lower mass ETGs. In many previous studies of the MASSIVE sample, the comparable ATLAS^{3D}

project (Cappellari et al. 2011, hereafter A3D), a volume limited survey within 42 Mpc, has been used as a comparison sample at the low mass end (Ma et al. 2014; Davis et al. 2016; Veale et al. 2017a). In this work, in order to study relations between IMF and galaxy properties, we seek a comparison sample where similar stellar population synthesis modeling exists over a comparable physical aperture.

Our main comparison sample comes from Conroy & van Dokkum (2012a, hereafter CvD) which consists of 34 galaxies in the SAURON sample (Bacon et al. 2001) and 4 galaxies in the Virgo cluster. As will be discussed in § 3, there are several differences in detailed methodology between this paper and CvD. However, both works focus on the central region of ETGs within an effective circular radius of $R_e/8$, and the M/L and α_{IMF} are constrained by the same spectral modeling tool. Therefore, the 38 ETGs in CvD are a natural comparison sample at lower stellar mass. The IMF measurements for ATLAS^{3D} galaxies (e.g. Cappellari et al. 2013a) also constrain the M/L and IMF in lower-mass ETGs, but through dynamical modeling, making CvD a more natural comparison sample. We use CvD to explore scaling relations between the IMF and galaxy properties. We also examine dynamical masses in § 5 and discuss the importance of matched apertures in comparing with dynamical masses that are necessarily measured over much larger spatial scale, given the apparently steep gradients in low-mass IMF slope. We adopt the A3D sample and dynamical masses from Cappellari et al. (2013a) for the latter discussion.

2.3. Data Collection

We present deep spectroscopy from Magellan/LDSS3 observations for 41 MASSIVE galaxies. The wide wavelength coverage (4000–10300Å) and high signal-to-noise (S/N) of our spectra enable measurements of kinematics, elemental abundances, age, and stellar IMF. The average S/N at 4500–5500Å and 8000–9000Å are $\langle S/N \rangle = 124\text{Å}^{-1}$ and $= 234\text{Å}^{-1}$ respectively.

Our targets were observed in eleven nights from August 2016 to March 2017 with the 1.0'' wide long slit on the LDSS-3 instrument at the Magellan Clay telescope: March 7th-9th, 2016, August 24th-26th, 2016 and March 22nd - 26th, 2017. The spectral resolution is $R = 1425$ and 1358 in VPH-Blue and Red. We derive the wavelength-dependent instrumental resolution from measurements of arc and sky lines to find, on average, $\sigma = 81$ and 82km s^{-1} in VPH-Blue and Red. The wavelength coverage is 3800–6200Å and 6000–10000Å in the VPH-Blue and VPH-Red grisms, respectively. A blocking filter, OG590, is included during the observation with the VPH-red grism to eliminate second order contamination at $\lambda > 7000\text{Å}$. Observations are taken in the 2×1 binning mode, resulting in a pixel scale of $0.378''/\text{pixel}$. The typical exposure times are $3 \times 800\text{s}$ in VPH-Blue, and $4 \times 600\text{s}$ with the VPH-Red grism for each target. The slit was not always oriented along the galaxy photometric major axis. We adopt the position angle measured in the Siena Galaxy Atlas Survey (Moustakas et al. 2021) and calculate the corresponding effective radius at the observed slit angle to ensure that the apertures cover the same fraction of R_e for all galaxies. Flat and arc exposures are taken in the afternoon prior to each observation night, and standard stars and bias exposures are taken during each observation night. All observations are read out in “fast” mode, with a readout noise of $3.5e^{-1}$.

We adopt distances for 19 galaxies in our sample based

⁵ This paper includes data gathered with the 6.5 meter Magellan Telescopes located at Las Campanas Observatory, Chile.

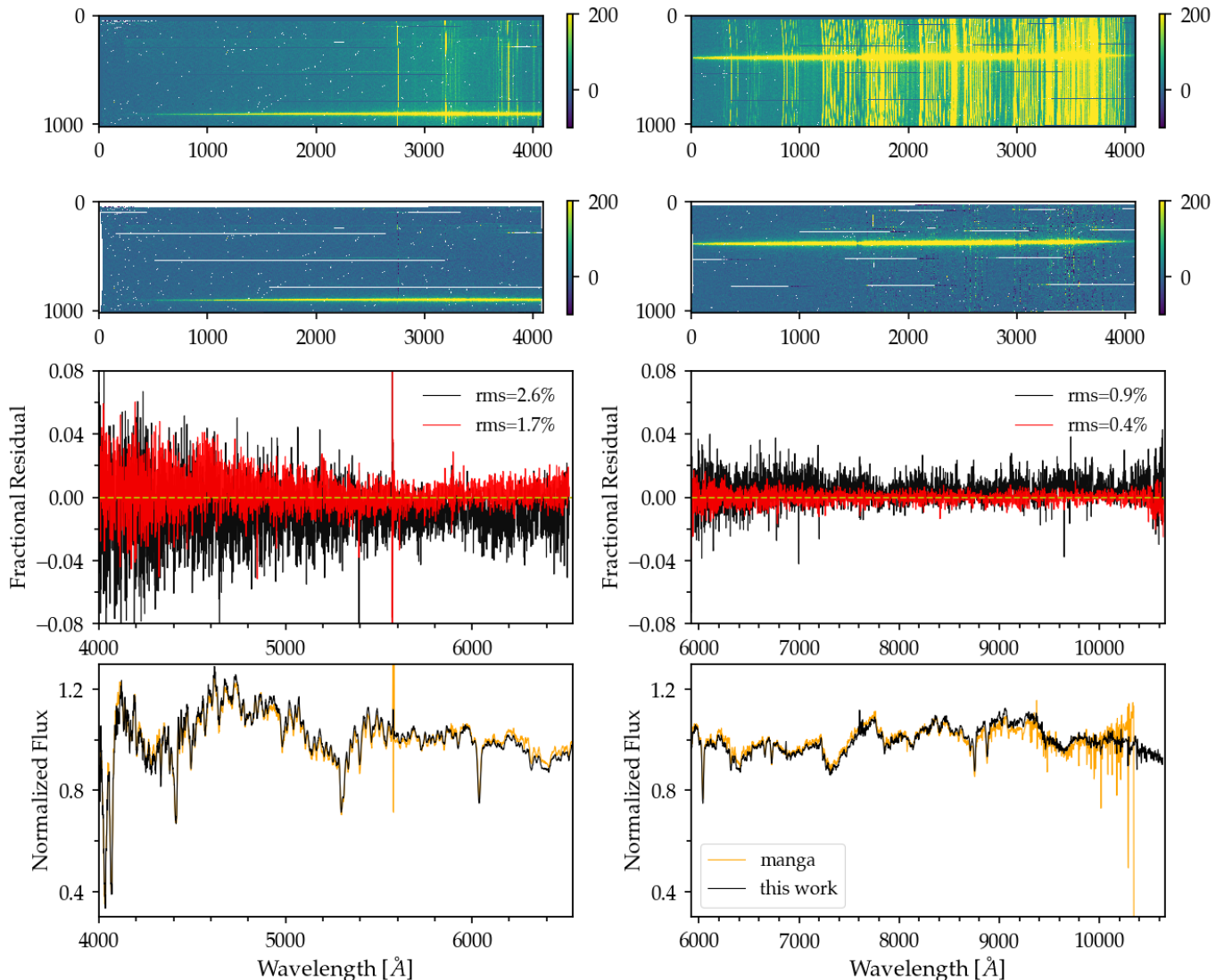


FIG. 1.— An illustration of the sky-subtraction performance with NGC 4839 as an example. Left and right panels show results from the blue and red spectrographs, respectively. Top two panels show the 2D images before and after sky subtraction. In the red, most sky emission lines are removed. The fractional sky-minus-sky residuals of a single exposure (black) and all exposures in one night (red, including four exposures in the blue and six exposures in red) are shown in the third row. The rms of fractional residual are marked at the top right corner. In the bottom panels, the flux-normalized spectrum of NGC 4839 assuming a circular aperture of $R_e/4$ is compared to a stacked spectrum in the same aperture observed by MaNGA. The fluxes are consistent with the MaNGA results and the residuals in the regions contaminated by sky emission lines are mostly clean.

on infrared surface brightness fluctuation measurement from Jensen et al. (2021). In addition, we utilize galaxy properties measured in previous MASSIVE Survey papers (Ma et al. 2014; Veale et al. 2018; Ene et al. 2020), including distances for other galaxies in the sample, foreground galactic extinction, and K -band photometry. For most targets, we adopt effective radii (R_e) in semi-major axis and K -band luminosity measured from observations with WIRCAM on the Canada France Hawaii Telescope (CFHT) (Quenneville et al., in prep). In brief, stacked images were produced using the WIRWOLF pipeline (Gwyn 2014) and elliptical isophotes were determined using ARCHANGEL. The contaminating sources are defined as pixels more than four standard deviations away from the mean of the intensity and are excluded. The intensity and its uncertainty are measured in each isophote, and the sky level is determined from the curve of growth. The half-light radii are measured as the radii containing half of the total light

through interpolation of the curve of growth.

The average ratio between R_e measured in (Quenneville et al., in prep) and adopted in previous works in the MASSIVE survey (Ma et al. 2014) (from 2MASS) is 1.17. For the remaining seven galaxies, we adopt the R_e used in previous MASSIVE papers, but multiple the radius by this ratio to keep consistency through the sample. On average the R_e along the semi-major axis of our sample is $\langle R_e \rangle = 7.2 \pm 2.8$ kpc, where the quoted error refers to the root-mean-square deviation. The calculation of SDSS- r band luminosity is based on R_e along the semi-major axis. We utilize the ellipse-fitting surface brightness profiles from the Siena Galaxy Atlas Survey (Moustakas et al. 2021) in the DESI Legacy Imaging Surveys where available, or SDSS `cmodel` r -band magnitude (Gunn et al. 1998; Abolfathi et al. 2018).

2.4. Data Reduction

We use an updated version of the data reduction pipeline by [Newman et al. \(2017\)](#). This version of the pipeline has been translated into Python and has major updates in wavelength calibration and sky subtraction. We briefly summarize the steps as follows and highlight the differences.

Raw data from the observations are stored in two files in FITS format from two independent amplifiers. The bias level is measured through the overscan regions, and is subtracted from the two frames separately. Data are then converted from ADU to electrons units using a gain of $1.67e^-/\text{ADU}$ and $1.43e^-/\text{ADU}$ in the two amplifiers respectively. After combining two frames, we get FITS files each containing an image of 4096×1024 pixels in the wavelength and spatial directions. The median of the bias exposures is subtracted from each calibration and science exposure.

Wavelength solutions are derived from the He, Ne, and Ar lamp exposures in both the blue and red cameras observed prior to each night of observation. In addition to the nightly lamp arc lines, we also make use of the sky lines from one science exposure by excluding ± 70 pixels from the galaxy center in the spatial direction, so that the wavelength range redder than 9000\AA is better sampled by the sky lines. For all exposures used for wavelength calibration, a background estimate based on the 2nd percentile of all pixel values in the image is subtracted. From the spectrum in the center, a set of bright lines are identified and matched with the arc (Ne, He, Ar) or sky-line locations. The lines are usually not aligned in the spatial direction. Therefore, the identification was first performed on the spectrum located in the center. For all other locations in the spatial direction, we take the curvature into account and allow a small overall offset of all line centers (no larger than 5 pixels) included in the fitting. Every 10 columns in the red and 5 columns in the blue are median combined and used to sample in the spatial direction. In this way typically we are able to locate 22 arc lines in each arc exposure, and 40 sky lines from science exposures in the red. For the 2D fitting, we follow steps similar to `PyPeIt` ([Prochaska et al. 2020](#); [Prochaska et al. 2020](#)). After locating the arc and sky lines at different spatial locations, we perform 2D Legendre-polynomial fitting. For the arc lines in the blue camera we use orders of 6 and 3 in the wavelength and spatial direction, respectively. For the red camera, we combine the arc and sky emission line measurements and fit them with orders of 6 in both the wavelength and spatial direction. This step gives us a two-dimensional wavelength solution map.

In addition, spectra are usually not perfectly aligned parallel to the CCD pixels. To trace the spectral distortion, we add two dithered exposures of the same galaxy to map the distortion perpendicular to the dispersion direction. In a pair of dithered exposures, galaxies are usually not located in the center, but in the top and bottom half of the CCD. In the combined image, we trace the locations of the two galaxy peaks every 5 pixels throughout the spatial directions. We then build a trace map by fitting 3rd and 5th order polynomials in the blue and the red, respectively. The above steps provide us two sets of coefficient arrays for the wavelength and trace solutions.

We took dome flat exposures using Quartz lamps in the afternoon prior to the science observations. A two-dimensional master flat for each night is constructed using the median of all flat exposures. We then model the lamp spectrum and divide that out to isolate the pixel-to-pixel sensitivity variations and the non-uniformity in the slit. To model the lamp spectrum, we first fit for a slit function which shows the variation

along the slit by performing an iterative one-dimensional 4th order b-spline fit to the median spatial profile of the central half pixels in the wavelength direction. With the spatial profile divided out, we fit for a one-dimensional lamp spectrum using the median spectrum in the central half pixels in the spatial direction using a cubic b-spline fit. We then construct a two-dimensional lamp spectrum using the wavelength solution. Dark pixels are identified and marked in this step. The final flat frame for normalization is derived by dividing the median flat by the two-dimensional model of the lamp spectra and then normalized by the median value. All science exposures are normalized by the final flat frame. Cosmic rays are identified and removed by `L.A.COSMIC` ([van Dokkum et al. 2012](#)). For each science exposure, the small wavelength zero-point correction is derived by fitting for the differences in a few sky line at all columns (5577.338\AA , 6300.304\AA in the blue, and 6300.304\AA , 9375.961\AA , 10418.363\AA in the red)

We follow sky subtraction procedures similar to the MUSE ([Weilbacher et al. 2020](#)) and MaNGA ([Bundy et al. 2015](#)) data reduction pipelines ([Law et al. 2016](#)). The regions used to fit for sky spectra are chosen to be ± 250 pixels away from galaxy centers, except for three very nearby galaxies in the Virgo cluster where we increase the threshold to ± 350 pixels. From the Siena photometry, the average r -band surface brightness at 250 and 350 pixels for all galaxies are 24.8 and 26.4 mag arcsec $^{-2}$. We divide the sky regions into continuum and sky emission line regions, and those in the sky emission line regions are further divided into several groups based on the origin of the sky emission lines following [Weilbacher et al. \(2020\)](#). The reason is that the sky emission lines scale similarly within the same group. Skylines with flux above 0.5% of the brightest sky line are considered in the scaling. Among these sky lines, we start with the group with the brightest total flux, and assume pixels within 3\AA from the emission line center belong to the group. The remaining pixels are assumed to be in the continuum region. A relative scaling factor array is then derived by comparing the 4σ -clipped mean flux of all pixels in the same group in different exposures. The scale factor array is normalized by the minimum before applied to all exposures.

To model the sky background for one exposure, we use the sky regions in the exposure itself and its two neighboring exposures. The sky is then modeled using a procedure similar to ([Law et al. 2016](#)): due to the wavelength correction in each exposure, the sky pixels in 3 exposures sample the sky spectra much better than a single exposure. We smooth the inverse variance spectra by a box car of width 100 pixels in the continuum, and 3 pixels within 3\AA of emission lines. This step helps prevent a bias towards lower values in the sky modeling. Then a sky model is constructed with an iterative two-dimensional b-spline function, with break points spacing of 1.0 pixel in the blue, and 0.7 in the red, and a third order polynomial in the spatial direction. The sky model for each exposure is then multiplied by the scaling factor in each emission line group and the continuum region.

In [Figure 1](#), we show our sky subtraction performance in one exposure of NGC 4839 in the red. Left and right panels show results in the blue and red spectrographs, respectively. The top two panels show the 2D exposures before and after sky subtraction, while the middle panel shows the 2D sky model. Note that in the red, most of the sky emission is removed. The third panel shows the fractional sky residuals as a function of wavelength. We randomly select 200 resid-

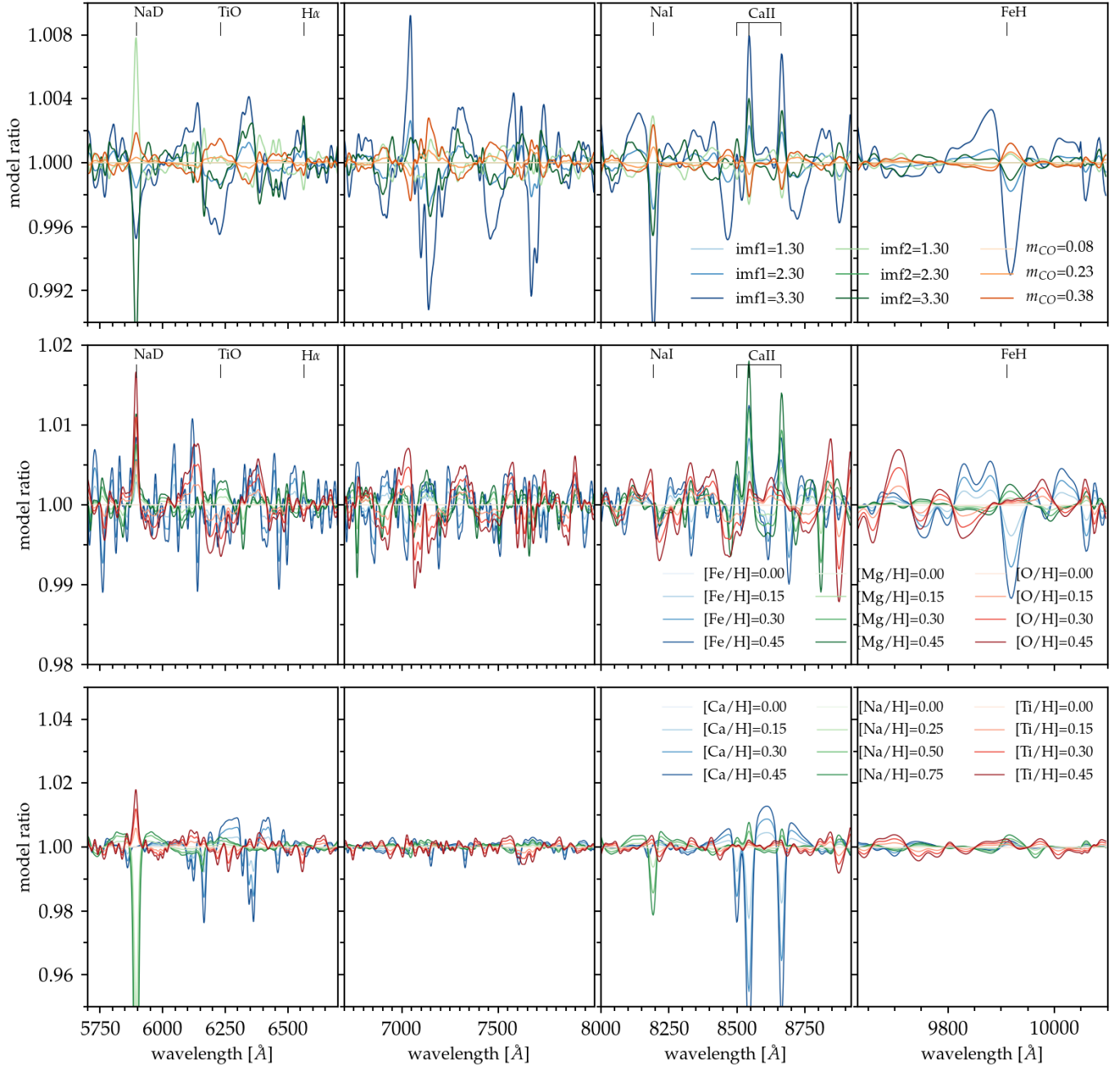


FIG. 2.— Illustration of model sensitivity to the change of stellar population parameters as a function of wavelength. Models are smoothed to $\sigma = 250 \text{ km s}^{-1}$. In all panels the reference model has solar abundances and a Kroupa IMF. The ratio between each model and the reference are normalized by a polynomial with one order per 100 \AA . In the top panels, imf1 and imf2 represent the IMF slopes below and above $0.5 M_{\odot}$ and m_{CO} represents the low mass cutoff. The top panels show the flux-normalized ratio between each model with parameters varied relative to the model with a Kroupa IMF ($\text{imf1}=1.3$, $\text{imf2}=2.3$, $\text{imf3}=0.08$). The middle and bottom panels show the regions that are sensitive to changes in the abundances of Fe, Mg, O, Ca, Na and Ti. Although in some regions it looks like an increase in imf1 and imf3 result in similar change of model ratio, e.g., NaD, TiO, NaI and CaT, the changes among different features (e.g. NaI, CaT and the Wind Ford band) have slight differences and in principle it can break their degeneracy.

ual spectra in the sky regions (regions that are ≥ 250 pixels away from galaxy centers), and plot the median residual as a fraction of the median sky spectra. The fractional residuals are less than 5% at all wavelengths. In the bottom panels, the flux-normalized spectrum of NGC 4839 assuming a circular aperture of $R_c/4$ is compared to a stacked spectrum in the same aperture observed by MaNGA DR8. The flux is consistent with the MaNGA results and the residuals in the regions contaminated by sky emission lines are low. Sky models and

sky subtracted exposures and the corresponding inverse variance array are all rectified based on the wavelength and spatial grids. Spectra are first linearly resampled with flux conserved to a common linear wavelength grid of 4096 pixels starting at 3774 \AA and 5923 \AA in the blue and red, respectively, and width of 0.6757 \AA and 1.156 \AA . They are then resampled onto a common grid in the spatial direction based on the trace solution. We note that there is a significant amount of scattered light in the far red with LDSS-3. This is primarily indicated

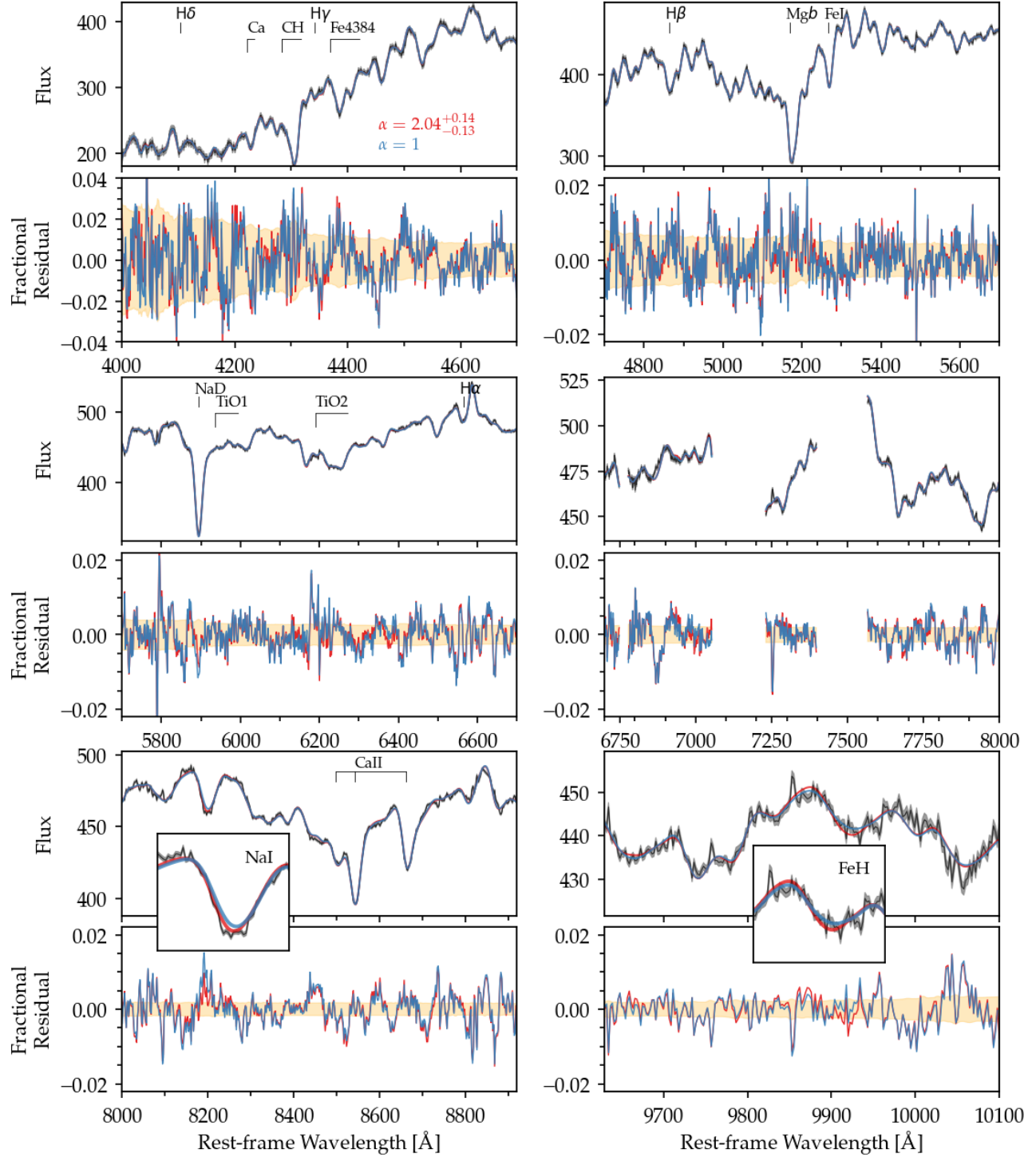


FIG. 3.— Comparison between two models of the spectrum of NGC 5490 extracted from an effective circular aperture of $R_e/8$. Data (black) and model flux are shown in the top panels, and the fractional residuals in the bottom panels. Our fiducial model has a flexible IMF with three parameters (low and high mass slopes, and a low mass cutoff) and is shown in red. A model with a fixed Kroupa IMF is shown in blue. The two models result in a ratio of IMF mismatch parameter of 2.04. Our best model reveals an IMF more bottom heavy than Salpeter. Note that the residuals from the fiducial model are noticeably smaller in the IMF sensitive features, especially around NaI, NaD, TiO, *Mgb* and the Wing-Ford band.

by the increasingly extended spatial profile around $1\ \mu\text{m}$. The scattered light cannot be perfectly removed and pixels near the Wing-Ford band are often contaminated.

2.5. Extraction

We use effective circular radii of $R_c/8$ (§ 2.2). To mimic the circular aperture, we assign different weights to pixels as a function of distance from the galaxy center, r . Specifically, all pixels within $0.5''$ have weights of unity and outer pixels are assigned with weight of $\pi \times r$. Standard stars are extracted in a radius of $4.0''$.

The standard stars used in this work are EG274, GD71 and LTT7987. To perform flux calibration, each standard star spectrum from the VizieR archive is divided from our standard star observations. Then the galaxy spectrum is normalized by the smoothed calibration spectrum. During spectral extraction, we assign weights to pixels in the spatial direction to mimic a circular aperture. The telluric correction is calculated for extracted galaxy spectra. We model and remove telluric absorption features by fitting atmospheric models using the MOLECFIT code, assuming the contributing molecular species are H_2O and O_2 . The bands used for telluric modeling are $6250-6300\text{\AA}$ in the blue, and $6820-6970\text{\AA}$, $7210-7330\text{\AA}$, $7590-7690\text{\AA}$, $8170-8360\text{\AA}$ and $9100-9400\text{\AA}$ in the red. The telluric correction derived is then used for other apertures.

3. SPECTRAL FITTING

We model the spectra using the absorption line fitter (`alf`, Conroy & van Dokkum 2012a; Conroy et al. 2014, 2018). We present the details of the modeling tool in § 3.1, then show the best-fit models and residuals, along with a comparison to fixed-IMF results, in § 3.2.

3.1. Modeling

`alf` enables full spectral stellar population modeling for stellar ages $> 1\text{ Gyr}$ and for metallicities from ~ -2.0 to $+0.25$. The Markov Chain Monte Carlo (MCMC) algorithm (`emcee`, Foreman-Mackey et al. 2013) is used in the exploration of parameter space. Currently `alf` adopts the MIST stellar isochrones (Choi et al. 2016) and utilizes a new spectral library (Villaume et al. 2017) that includes continuous wavelength coverage from $0.35-2.4\ \mu\text{m}$. It also utilizes the theoretical response functions that were computed using the ATLAS and SYNTH programs (Kurucz 1970, 1993). The theoretical response functions tabulate the effect on the spectrum of enhancing each of 18 individual elements.

There are 36 free parameters involved in the fitting: galaxy kinematics (radial velocity, and velocity dispersion), a two-burst star formation history (two ages and a mass fraction), and stellar populations, including the overall metallicity ($[Z/H]$) and 18 individual element abundances (Fe, Mg, O, C, N, Na, Si, K, Ca, Ti, V, Cr, Mn, Co, Ni, Sr, Ba, Eu). In the two-burst model, the young component has as a prior an upper age limit of 3 Gyr, while the older component prior has an upper limit of 14 Gyr. Both have a lower limit on their age of 0.5 Gyr. We adopt flat priors from $500-10500\ \text{km s}^{-1}$ for recession velocity, $10-1000\ \text{km s}^{-1}$ for velocity dispersion, and $-1.8-0.3$ for $[\text{Fe}/\text{H}]$. The priors are zero outside these ranges. The prior ranges for elemental abundances are $-0.3-0.5$ except for $[\text{Na}/\text{H}]$, which is $-0.3-1.0$.

There are several possible forms for the stellar IMF in `alf`. In our fiducial model, we use `alf` to fit three parameters for

the stellar IMF: two logarithmic slopes in $dn/dm \propto M^{-\gamma}$, in the mass ranges $0.08M_\odot < M < 0.5M_\odot$ (`imf1`), $0.5M_\odot < M < 1.0M_\odot$ (`imf2`), and a low mass cutoff (`imf3`). At $M \geq 1.0M_\odot$, the slope is fixed to the value of a Salpeter slope, $\gamma = 2.3$. The priors on `imf1` and `imf2` are both flat with ranges of $0.5 \leq \text{imf1}/\text{imf2} \leq 3.5$, and $0.08M_\odot \leq \text{imf3} \leq 0.4M_\odot$. A Kroupa IMF with `imf1`=1.3 and `imf2`=2.3 is used as a reference. From the M/L posterior, the IMF mismatch parameter, $\alpha_{\text{IMF}} \equiv (M/L)/(M/L)_{\text{Kroupa}}$, is also calculated. This parameter refers to the best-fit M/L normalized by the M/L based on the reference IMF, and indicates how much the best-fit IMF deviates from the reference IMF. Since M/L is sensitive not only to the IMF, but also age, metallicity, etc, this normalization is helpful since α_{IMF} is only sensitive to the IMF. In this work the Salpeter IMF is assumed to be in the form of a single power law with a slope of 2.35 over a mass range of $0.1-100M_\odot$, which is different from what is defined in Salpeter (1955). The IMF mismatch parameter of the Salpeter IMF is assumed to be $\alpha_{\text{IMF}} \approx 1.55$.

Several ‘‘nuisance’’ parameters are included: hot star components, emission lines (H, [O II], [O III], [S II], [N I], and [N II]), and an error jitter term to correct the observational uncertainties. For each spectrum, the continuum is first normalized by a polynomial fitted to the ratio between model and data. The polynomial has an order of $(\lambda_{\text{max}} - \lambda_{\text{min}})/100\text{\AA}$. We fit in five separate wavelength intervals: $0.4-0.47, 0.47-0.57, 0.57-0.67, 0.675-0.80, 0.80-0.892$ and $0.963-1.01\ \mu\text{m}$. Pixels with strong telluric contamination in the following ranges are masked out in the observed frames: $0.717-0.735\ \mu\text{m}$, $0.686-0.689\ \mu\text{m}$ and $0.752-0.769\ \mu\text{m}$.

Figure 2 illustrates the sensitivity of the model to the change in parameters, as a function of wavelength. Models with varying parameters are compared to a reference model with solar stellar populations and a Kroupa IMF. All models are smoothed to $\sigma = 250\text{ km s}^{-1}$ in this figure. The ratio between each model and the reference are normalized by a polynomial with an order of $(\lambda_{\text{max}} - \lambda_{\text{min}})/100\text{\AA}$. In the top panels, `imf1` and `imf2` represent the IMF slopes below and above $0.5M_\odot$ and m_{co} represents the low mass cutoff. Figure 2 illustrates the relative wavelength sensitivity of a few parameters. For example, an increase in `imf1`, `imf2` or $[\text{Na}/\text{H}]$ will be reflected in a deeper NaI feature, suggesting that the NaI feature is sensitive to more than just the Na abundance. In addition, the change caused by a varying low-mass cutoff (`imf3`) at different wavelengths has a different amplitude compared to the changes caused by a varying IMF slope at $0.08-0.5M_\odot$ (`imf1`), or $0.5-1.0M_\odot$ (`imf2`), indicating that the effect due to `imf3` cannot be simply compensated by `imf1` or `imf2`.

Since the goal of this work is to study global variations in the IMF and their connection with stellar populations, CvD is our main comparison sample (§ 2.2). Although we are using the same method as CvD, there are some differences in the details and we list them as follows: We use a version of `alf` with updated stellar libraries (Villaume et al. 2017), stellar isochrones (Choi et al. 2016) and response functions. Details of the updates are summarized in Conroy et al. (2017). Also, we include wavelength intervals of $0.57-0.67\ \mu\text{m}$ and $0.67-0.80\ \mu\text{m}$, which are not included in CvD. As shown in Figure 2, the additional wavelength intervals in our work indicate that we have more information to constrain the IMF and the abundances of elements such as Mg, O, Ti. We do not include the nuisance parameters `logm7g` and `teff` as free parameters in the fitting. `logm7g` and `teff` represent the

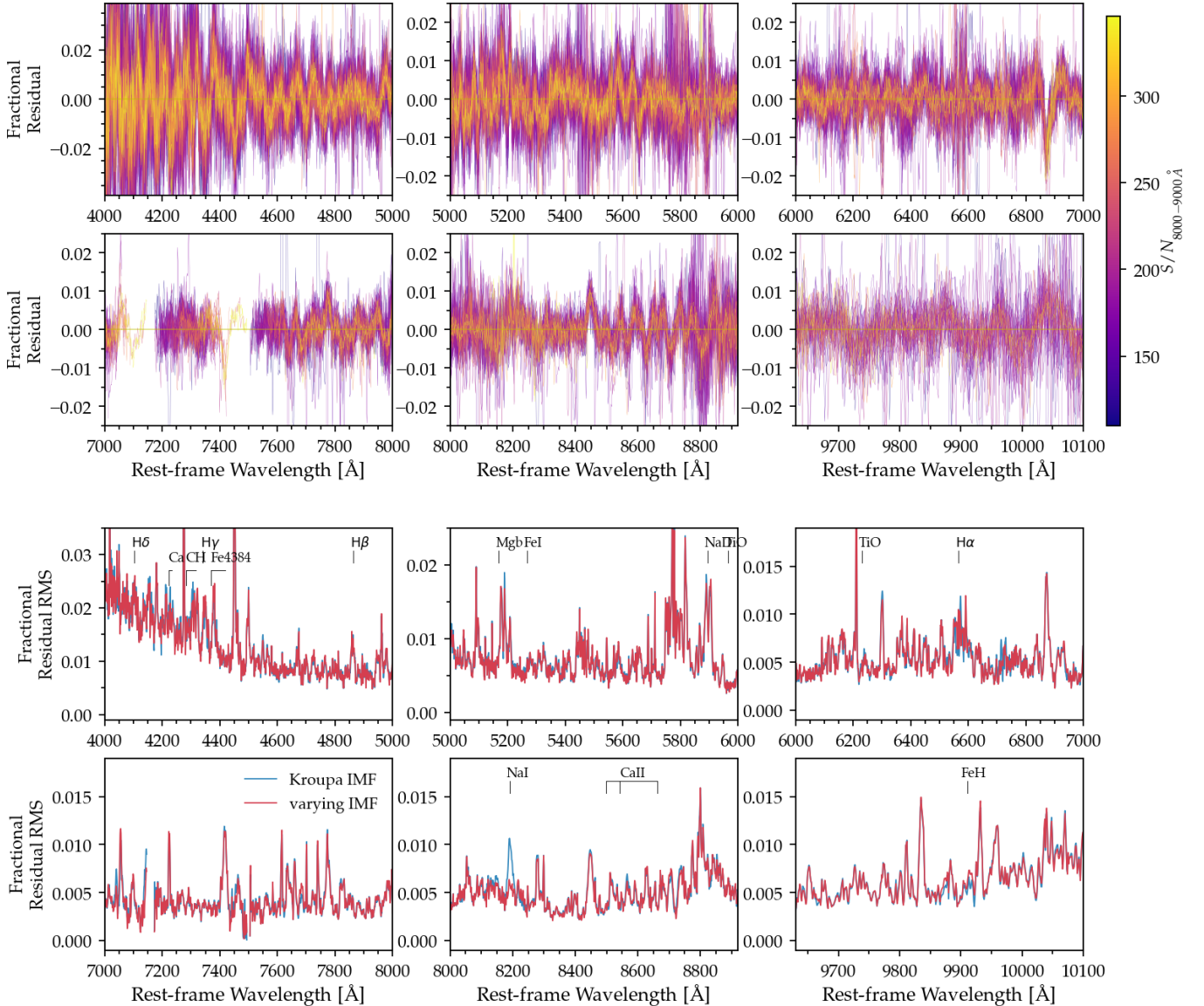


FIG. 4.— Top: Fractional residuals from the fiducial IMF model (two power-law IMF + low cutoff mass) for all galaxies in our sample. Colors indicate the mean S/N in $8000-9000\text{\AA}$. On average the fractional residuals are smaller than 2%. For spectra with $S/N > 300$, the fraction residual is better than 1% in the red. Bottom: A comparison of fractional residual rms of all 41 galaxies from fitting with a fixed Kroupa IMF, and the fiducial model. A model with a fixed Kroupa IMF creates much larger residuals in several regions, specifically around NaI.

light at $1\mu\text{m}$ contributed by an M7III giant star, and the shift in T_{eff} relative to the fiducial isochrones, respectively. They were introduced for systematics testing in an early version of `alf` when the isochrones were not metallicity dependent and are not useful in the current version. `logtrans` represents the strength of the atmospheric transmission function for H_2O and O_2 together. Since we have corrected for the atmospheric transmission function from H_2O and O_2 separately using `MOLECFIT`, `logtrans` is not included in the fit. These differences make our model setup more comparable to Newman et al. (2017).

3.2. Best-fit Models and Residuals

In our default IMF model, the IMF is described by three parameters: low (`imf1`) and intermediate mass (`imf`) slopes and a low cut-off mass (`imf3`). In contrast, a Kroupa IMF has a low mass slope of `imf1`=1.3 and an intermediate mass slope of `imf2`=2.3. Since `alf` uses all available pixels in the

spectra, instead of single spectral absorption features, changes in parameters are not all visibly prominent in the residuals. However for galaxies in our sample, the differences between models using the flexible (default) IMF or a fixed Kroupa IMF are always obvious, as fixing the IMF to the Kroupa form fails to describe all of the spectral features, especially the gravity-sensitive features.

We use one galaxy, NGC 5490, as an example and show a comparison between the two models in Figure 3. The spectrum has a mean $S/N = 296\text{\AA}^{-1}$ from $8000-9000\text{\AA}$ in the rest-frame. The best-fit model spectrum from our fiducial model, and the corresponding residuals, are shown in red. The results from a fixed Kroupa IMF are shown in blue. The α_{IMF} from the posterior of our fiducial model is $\alpha_{\text{IMF}} \approx 2.0$, indicating that the stellar IMF in the central region of NGC 5490 is more bottom heavy than Salpeter. Comparing the differences in the residuals, the main difference is that the residuals from

our fiducial model are noticeably smaller in the IMF sensitive features such as NaI, NaD and FeH. By forcing the IMF to a Kroupa form, `alf` tries to mitigate mismatches by changing abundance ratios in key features. For this particular galaxy the abundances of Fe, N, Ca, Ti are shifted to lower values by at least 1σ , and [Na/H] and $\log(\text{age})$ are shifted to higher values by $\sim 2\sigma$. NaI in particular is obviously under-fit by the Kroupa model. The [Na/H] abundances are 0.57 and 0.61 in our fiducial and Kroupa model. In other words, an increase in [Na/Fe] abundance is not enough to describe the strong NaI feature if we choose to force the IMF to be Kroupa. The shift in abundances by forcing the IMF to be Kroupa is consistent with what is shown in Figure 2, e.g., a decrease in [Ca/Fe] and increase in [Na/Fe] are induced to compensate the decrease of IMF slopes. Comparing the results from forcing the IMF to Kroupa with that from our fiducial model for the whole sample, on average, [N/Fe], [Ti/Fe], [Ca/Fe] are underestimated by 0.03, 0.02 and 0.02 dex, respectively. [Na/Fe] and [O/Fe] are overestimated by 0.02 and 0.05 dex, respectively. Although the sensitivities of IMF parameters and elemental abundances follow similar trends in some regions of the spectra (e.g., from Figure 2), Figure 3 demonstrates that `alf` is able to break the possible degeneracy especially with the information from gravity-sensitive features.

In the top sub-panel of Figure 4, we show the fractional residuals for all of the galaxies in our sample using the fiducial model. Colors indicate the median S/N of each spectrum at 8000–9000 Å. The mean S/N of all spectra in our sample is $\langle S/N \rangle = 234 \text{Å}^{-1}$. The general trend is that galaxies with higher S/N have fractional residuals closer to zero. Overall the residuals are smaller than 1% in the red. We notice that there are some wavelength dependent patterns in the residuals in the rest-frame. They are present in both low and high S/N spectra. This indicates that such patterns do not depend on data reduction or telluric modeling, and are more likely caused by the mismatch between the galaxy spectra and the model (van Dokkum et al. 2017).

In the bottom sub figure, we compare our fiducial model with the residuals from fixing the IMF to Kroupa. On average in the MASSIVE sample $\langle \alpha_{\text{IMF}} \rangle = 1.84 \pm 0.43$. These panels show the quadratic mean of fractional residual over all 41 galaxies as a function of wavelength. The residuals from our fiducial and reference models are shown in red and blue, respectively. A model with fixed Kroupa IMF results in much larger residuals in several regions: NaD, H α , region around TiO features and NaI. Despite the issue with scattered light in the far red, the Wing-Ford band provides an important constraint on both the stellar IMF and the Fe abundance so it is included in the fitting. On average, the Kroupa model tends to over-estimate the [Na/H] and under-estimate the abundances of Fe, Ca and Ti.

4. RESULTS

We present our main results in this section. In § 4.1 we describe the procedures to derive dynamical mass, stellar masses, and the effective stellar mass density. In § 4.2 we present the central properties of galaxies in our sample: their stellar populations and stellar IMF. We present correlations between stellar populations and other galaxy properties for our sample alone in § 4.3 and including the low-mass comparison sample in § 4.4. In § 4.5 we show multivariate linear regression involving α_{IMF} and stellar populations. In § 4.6 we briefly mention the relation with environment.

4.1. Dynamical Mass, Stellar Mass and Stellar Surface Density

The dynamical masses are calculated based on an empirical relation $M_{\frac{1}{2}\text{dyn}} = \beta \sigma_e^2 R_e / G$ presented in Cappellari et al. (2006, 2013b). We use r -band photometry from the Siena Galaxy Atlas (Moustakas et al. 2021). For galaxies in our sample, the Siena Galaxy Atlas has an average 5- σ PSF detection depth in r -band of 26.19 AB mag, significantly deeper than the SDSS r -band photometry. We refer to the SDSS- r -band filter as the r filter throughout the paper, and assume $r_{\text{SDSS}} = r_{\text{DECAM}} + 0.0381$ mag when calculating the luminosity based on Siena photometry. The mean offset between the luminosity from Siena and the SDSS `cmodel` photometry is $\Delta \log(L_r/L_\odot) = 0.06$, suggesting that the luminosity from Siena is on average 14% higher than SDSS.

In order to compare directly with the ATLAS^{3D} sample, we adopt the relation given by Cappellari et al. (2006), with $\beta = 2.5$, in the following sections. We note that there are three systematic effects that could cause a shift in β for our sample. First, as noted, our photometry is systematically deeper than the SDSS photometry used by Cappellari et al. (2013a). Second, the methods in deriving R_e are different. Third, our sample is dominated by slow rotators, unlike the vast majority of the ATLAS^{3D} sample (Veale et al. 2017b), and therefore may have systematically different dynamical masses for the same σ and R_e . With $\beta = 2.5$, the mean dynamical mass of galaxies in our sample is $(\log(M_{\text{dyn}}/M_\odot)) = 11.66 \pm 0.18$. The dynamical masses are shown in Column 4 of Table 1.

Our goal is to compare the dynamical and stellar population-based masses, and for this we need an M_*/L within R_e . To estimate the luminosity-weighted M_*/L within R_e , we first obtain M_*/L by modeling spectra extracted in effective circular apertures of $R_e/8, R_e/4$ and $R_e/2$. Most galaxies in our sample have a declining M_*/L_r with increasing radii. We will explore M_*/L gradients within individual galaxies in more detail in an upcoming paper. Since spectra from smaller aperture have higher S/N compared to the extraction in R_e and the high S/N is important for the M/L measurement, for now the luminosity-weighted M/L within R_e is derived from a linear extrapolation of $\log R - \log(M_*/L)_r$ at $R_e/8, R_e/4$ and $R_e/2$. The stellar masses are calculated using the luminosity from the Siena photometry where available or SDSS `cmodel` (§ 2), and the results are shown in Table 1. We discuss the comparison between dynamical mass and stellar mass within R_e in § 5.

When we discuss the effective stellar surface mass density (Σ) within R_e , $\Sigma = M_*/(2\pi R_e^2) = (M_*/L) \times L/(2\pi R_e^2)$, we use the $(M/L)_{\text{Kroupa}, R_e}$, the mass-to-light ratio assuming a fixed Kroupa IMF, in order to discuss the relation between Σ_{Kroupa} and α_{IMF} . We do not use the best-fit M/L within R_e . The reason is that since $\Sigma = M_*/(2\pi R_e^2) = (M/L) \times L/(2\pi R_e^2) = \alpha_{\text{IMF}, R_e} \times (M/L)_{\text{Kroupa}} \times L/(2\pi R_e^2)$, and the best-fit surface density from our fiducial model is actually $\Sigma = \alpha_{\text{IMF}, R_e} \times \Sigma_{\text{Kroupa}}$, Σ based on the best-fit M/L will inevitably show a correlation with the extrapolated α_{IMF} within R_e , and bring any discussion about Σ and α_{IMF} into question. Therefore we choose to use the estimated M/L within R_e assuming a Kroupa IMF in order to exclude the effect of α_{IMF, R_e} when discussing the relation. We note that using a Kroupa IMF underestimates the stellar mass surface density and we will briefly discuss the differences brought with this assumption in later sections. We also note the difference from the the stellar mass calculation

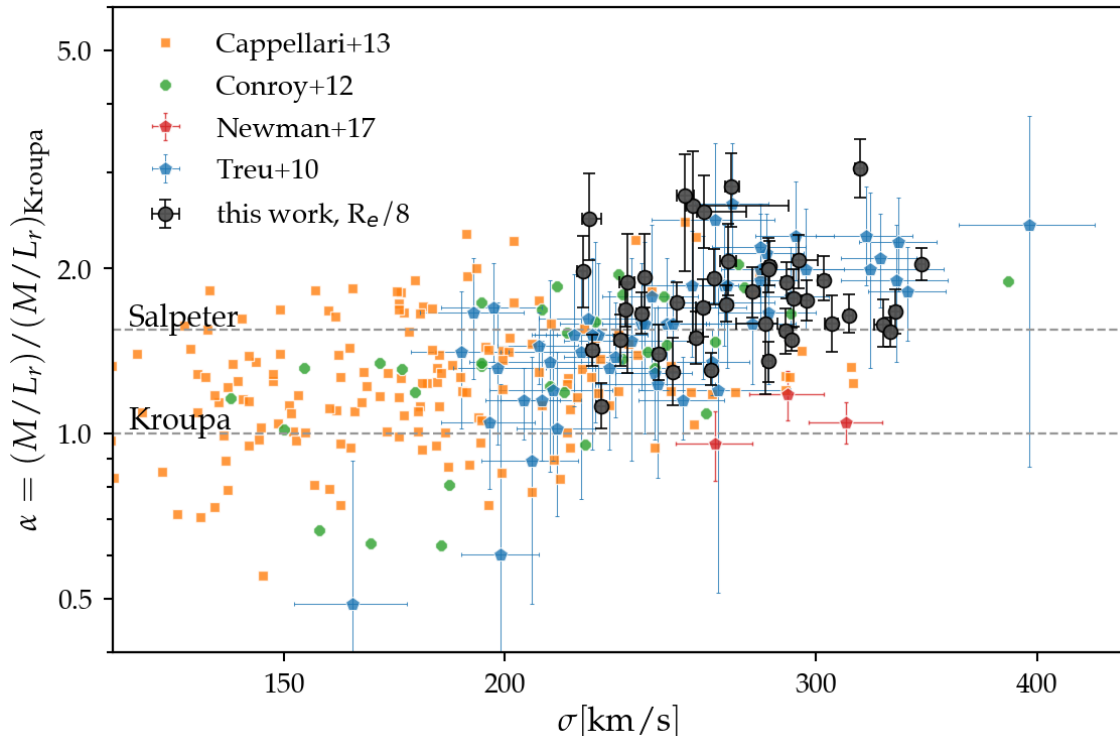


FIG. 5.— The IMF mismatch parameter, α_{IMF} , as a function of galaxy central velocity dispersion in this work (black) and previous studies based on SPS (CvD), dynamical modeling (A3D), and strong lensing (Newman et al. 2017; Treu 2010).

(presented in Table 1, Table 2, and Figure 7) which uses the best-fit M/L .

4.2. Central Properties of Massive Early-type Galaxies

The 41 early-type galaxies in our sample are among the most massive galaxies in the local universe. These galaxies have a mean central velocity dispersion of $\langle\sigma_c\rangle = 278 \pm 30 \text{ km s}^{-1}$ (Veale et al. 2017b), an average velocity dispersion within R_e of $\langle\sigma_e\rangle = 255 \pm 28 \text{ km s}^{-1}$, and an average stellar mass of $\langle\log(M_*/M_\odot)\rangle = 11.67 \pm 0.18$.

We focus on the stellar population properties of individual galaxies within $R_e/8$ throughout this work. Table 1 lists the stellar populations and stellar IMF within $R_e/8$ through detailed full spectral modeling. The error bars indicate the 16th and 84th percentiles of the posterior distributions. Galaxies in our sample cover a relatively narrow velocity dispersion ($\langle\sigma\rangle = 272 \pm 32 \text{ km s}^{-1}$), stellar and dynamical mass range. Here we list the mean values of the whole sample for some properties that are not included in Table 1: $\langle[\text{C}/\text{Fe}]\rangle = 0.21 \pm 0.04$, $\langle[\text{N}/\text{Fe}]\rangle = 0.17 \pm 0.09$, $\langle[\text{Ca}/\text{Fe}]\rangle = 0.06 \pm 0.02$, $\langle[\text{Si}/\text{Fe}]\rangle = 0.13 \pm 0.05$, $\langle[\text{Ti}/\text{Fe}]\rangle = 0.15 \pm 0.06$. We also note that the best-fit $[\text{Na}/\text{Fe}]$ is super-solar for all galaxies, with an average value of $\langle[\text{Na}/\text{Fe}]\rangle = 0.44 \pm 0.10$. We estimate the total metallicity using the equation from Thomas et al. (2002): $[\text{Z}/\text{H}] = [\text{Fe}/\text{H}] + 0.94 \times [\text{Mg}/\text{Fe}]$. The mean total metallicity over our sample is $\langle[\text{Z}/\text{H}]\rangle = 0.38 \pm 0.04$. Galaxies in our sample are dominated by the old stellar population with a mean young fraction of only 0.28%.

In Figure 5 we present α_{IMF} as a function of σ directly measured from the extracted spectra within $R_e/8$. We compare our results with α measurements from the recent literature using different methods: α_{IMF} of A3D galaxies within R_e based on the best-fitting JAM model and NFW halo as a function of central σ ($R_e/8$) (Cappellari et al. 2013b), central α_{IMF} as a

function of central σ ($R_e/8$) of 38 galaxies in (Conroy & van Dokkum 2012b) based on full spectral modeling, results of 56 ETGs based on joint analysis of lensing and dynamical modeling (Treu 2010), and stellar M/L measured based on lensing and an assumption of dark matter fraction from EAGLE simulation in the SINFONI Nearby Elliptical Lens Locator Survey (Newman et al. 2017). The reference IMF have been all converted to Kroupa. A general trend that α_{IMF} increases with increasing σ have been reported in Conroy & van Dokkum (2012b), Cappellari et al. (2013b) and Treu (2010), and our results are in good agreement with the trend.

Figure 6 shows the stellar population and IMF parameter fits as a function of σ . Error-bars indicate the 16th and 84th percentiles and points indicate the median of the posterior distribution. Colors indicate the stellar mass. Since our sample contains only the most massive galaxies and covers a limited dynamic range, we complement our sample with low mass galaxies from CvD (see § 2.2). Their results are shown as green dots in Figure 6. There is an apparent offset in $[\text{Fe}/\text{H}]$ between our sample and CvD for galaxies in the regime of overlap with $\sigma \sim 220$ to 260 km s^{-1} . The model used in this work utilizes an updated stellar library (Villaume et al. 2017) with wider metallicity coverage. Therefore the discrepancy could be due to the difference in models. Moreover, since $[\text{Fe}/\text{H}]$ has a well-known gradient with radius, differences in R_e measurements could add to the apparent discrepancy.

In our sample, the average M/L in the r and g bands are $\langle M/L_r \rangle = 6.37 \pm 1.41 M_\odot/L_\odot$, and $\langle M/L_i \rangle = 4.35 \pm 0.94 M_\odot/L_\odot$, respectively. We also calculate the α_{IMF} mismatch parameter to indicate how much the IMF of our best-fit model deviates from our reference IMF. We take the Kroupa IMF as our reference, and find an average α_{IMF} of $\langle\alpha_{\text{IMF}}\rangle = \langle(M/L)/(ML)_{\text{MW}}\rangle = 1.84 \pm 0.43$. On average, the massive galaxies in our sample have an IMF that is more

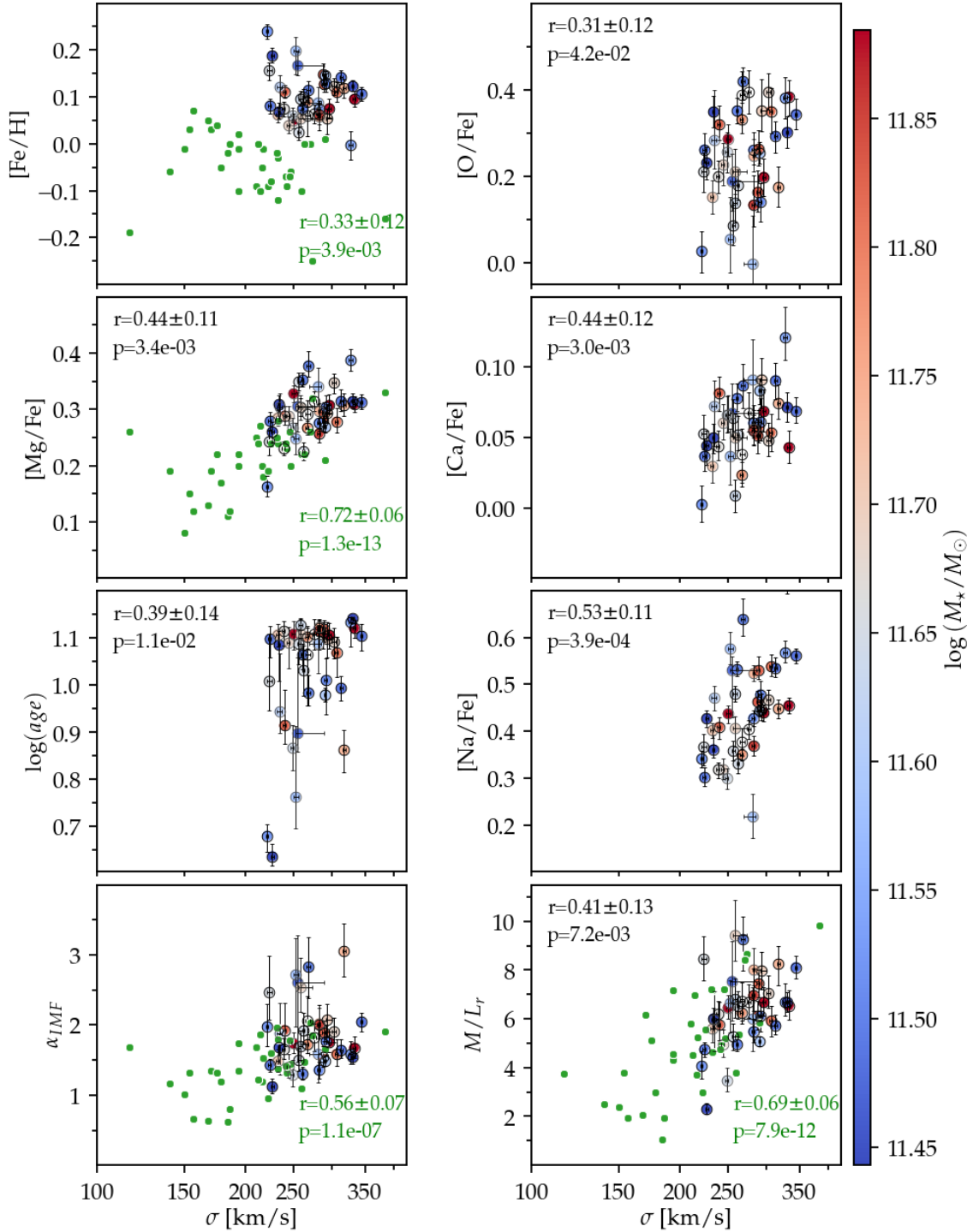


FIG. 6.— From top left to bottom right: [Fe/H], [Mg/Fe], $\log(\text{age})$, IMF α -mismatch parameter, [O/Fe], [Ca/Fe], [Na/Fe] and M/L_r as a function of σ for all galaxies in our sample. All properties are luminosity weighted within R_e . Colors indicate the stellar mass. Results from CvD (green) are included as a comparison for available parameters. Pearson correlation coefficients and the 1σ uncertainty are shown when the corresponding p -value is smaller than 5%. For our sample alone and the combined sample they are shown in black and green, respectively.

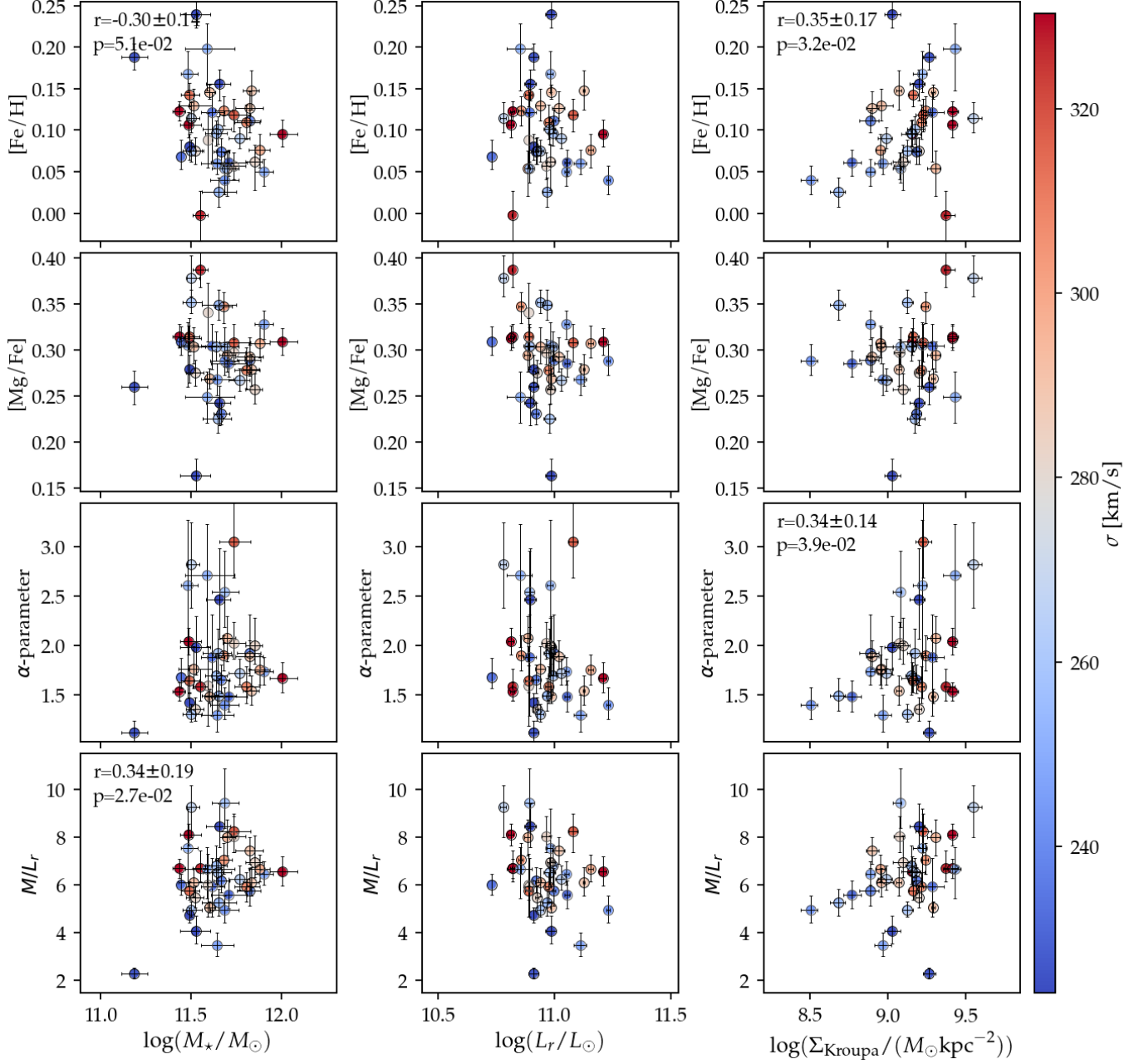


FIG. 7.— From top left to bottom right: [Fe/H], [Mg/Fe], IMF α -mismatch parameter and M/L_r as a function of logarithmic stellar mass, luminosity and effective stellar surface density for all galaxies in our sample. Pearson correlation coefficients and the 1σ uncertainty are shown when the corresponding p -value is smaller than 5%.

bottom heavy than one with a Salpeter slope, which has an $\alpha_{\text{IMF}} = 1.55$. All of the galaxies have a stellar IMF that is more bottom heavy than Kroupa (Table 1). Galaxies in our sample span a large range of α_{IMF} from $1.12^{+0.11}_{-0.10}$ (NGC 1700) to $3.05^{+0.39}_{-0.36}$ (NGC 4555). The sample standard deviation is 0.43, much larger than the average measurement uncertainty of 0.26, therefore the scatter in α_{IMF} is unlikely to be explained by measurement uncertainty alone. We will discuss possible drivers for the scatter in the following sections.

4.3. Stellar Population Scaling Relations in the MASSIVE Sample

In Figure 6 and Table 2 we present the stellar population and IMF parameters as a function of σ . We calculate Pearson correlation coefficients (r) between σ and all the stellar population or IMF parameters. We calculate the p -value for each correlation, which is the probability that the correlation is produced by an uncorrelated system. The parameter pairs with a p -value smaller than 5% are shown in black in the corresponding panels, where the uncertainty comes from 1000 bootstrap samples. The correlations measured based on the combined sample are shown in green.

Table 2 shows the correlation between two sets of variables. The first set includes stellar populations and the stellar IMF. The second set includes σ , stellar mass and dynamical mass, luminosity, and effective stellar surface density, and others. Based on the p -values, significant correlations are marked with an asterisk. For galaxies in our sample, we see mild positive correlations between $\log(\sigma)$ and the following parameters: [Mg/Fe], [O/Fe], [C/Fe] and [Na/Fe], as shown in Figure 6.

The trend that metallicity and [Mg/Fe] in ETG centers increase with increasing galaxy velocity dispersion has been shown in previous literature (e.g., Trager et al. 2000; Worthey & Colobert 2003; Thomas et al. 2005; Conroy et al. 2014). Within our sample there is no strong positive correlation between $\log(\sigma)$ and [Fe/H]. This could be due to the intrinsic scatter in [Fe/H] at the high mass end and our limited dynamical range. In addition, aperture effects could also wash out trends between σ and [Fe/H] since there is a strong negative [Fe/H] gradient within galaxies. [Fe/H] could be sensitive to the choice of aperture and the measurement of R_e .

In addition, we note that the correlations between σ and the following parameters are not included in the table or figure: [C/Fe]– $\log(\sigma)$: $r = 0.49 \pm 0.12$; [N/Fe]– $\log(\sigma)$: $r = 0.27 \pm 0.15$; [Si/Fe]– $\log(\sigma)$: $r = 0.12 \pm 0.17$. Despite the limited dynamic range, we found that [Mg/Fe], [C/Fe], [Ca/Fe] all increase within increasing σ and they are consistent with previous studies (e.g. Graves et al. 2007; Thomas et al. 2010; Johansson et al. 2012; Greene et al. 2015; Conroy et al. 2014). The trends of increasing abundances with increasing σ for O, Na are consistent with Conroy et al. (2014). [C/H] and [O/H] are strongly correlated in our sample with $r \approx 0.87$.

Although all galaxies in our sample have an IMF that is bottom heavier than Kroupa, there is a large scatter in α_{IMF} , and basically no correlation between $\log(\sigma)$ and α_{IMF} . Some of the correlations involving the IMF are shown in Figure 7. Within our sample, the effective stellar mass surface density ($\log(\Sigma_{\text{Kroupa}})$) (Table 2) and the total metallicity ([Z/H], Table 3) appear to positively correlate with $\log(\alpha_{\text{IMF}})$ with $r = 0.34 \pm 0.14$ and $r = 0.25 \pm 0.17$, respectively. There are moderate correlations in $\log(\Sigma)$ –[Fe/H] and $\log(\Sigma)$ –[Z/H] of $r = 0.34 \pm 0.17$ and $r = 0.46 \pm 0.12$, respectively, indicating

that in our sample, more compact galaxies are more metal rich and have a bottom-heavier IMF. We do not see any significant correlations between $\log(\alpha_{\text{IMF}})$ and [Mg/Fe], [O/Fe], [Ca/Fe] or [Ti/Fe] within our sample. The correlation with [Na/Fe] is moderate (Table 3). We note that when calculating Σ_{Kroupa} we adopt the assumption of a Kroupa IMF, which underestimates the stellar mass (§ 4.1). When we use the stellar mass calculated in our fiducial model (adopting an M/L extrapolated to R_e), the $\log(\Sigma)$ – $\log(\alpha_{\text{IMF}})$ correlation becomes more significant, with $r = 0.47 \pm 0.10$, $p = 0.4\%$. There is suggestive evidence that galaxy compactness might be an important property related to IMF variation.

The galaxies with the most bottom-heavy IMF in Figure 7 have moderate stellar mass and luminosity, but typically all have high effective stellar mass surface density, i.e., their distinguishing feature is their compactness instead of how massive they are. We will study how compactness affect the local or global α_{IMF} in detail in an upcoming paper. The effective surface density, Σ , requires a measurement of both R_e and L , which cannot be done uniformly across the two samples. Therefore our analysis of trends with Σ is limited to the MASSIVE sample. Since there is an overall trend that the IMF becomes bottom heavier in more massive galaxies (§ 4.4), we are also interested in whether the correlation with IMF within our sample is driven by $\log(\sigma)$. The partial correlation within the MASSIVE sample in $\log(\Sigma)$ – $\log(\alpha_{\text{IMF}})$ is $r = 0.36$, $p = 0.04$ when holding $\log(\sigma)$ and [Mg/Fe] constant, indicating the connection between $\log(\Sigma)$ and $\log(\alpha_{\text{IMF}})$ is significant and independent of $\log(\sigma)$ and [Mg/Fe]. In the rightmost column of Table 3 we present the partial correlation coefficients by fixing the effect of $\log(\sigma)$, which is $r \approx 0.25$ for [Z/H]– $\log(\alpha_{\text{IMF}})$ and $r \approx 0.36$ for $\log(\Sigma)$ – $\log(\alpha_{\text{IMF}})$, suggesting these positive correlations are not driven by galaxy central velocity dispersion.

In summary, within our sample, there is no significant correlation between α_{IMF} and σ or [Mg/Fe]. Both [Z/H] and $\log(\Sigma)$ show moderate positive correlations with α_{IMF} , and $\log(\Sigma)$ is moderately correlated with [Z/H], suggesting that they may be both responsible to the IMF variation within our sample

4.4. Stellar Population Scaling Relations in the Combined Sample

We present the correlations in the combined sample in Figure 8 and Table 3. In Figure 8, colors indicate the effective stellar mass surface density. Pearson correlation coefficients are shown in green at the top right corner of each panel for the combined sample. By including galaxies with lower σ from CvD, we find moderate positive correlations between $\log(\alpha_{\text{IMF}})$ and $\log(\sigma)$, [Mg/Fe], and [Z/H]. Among them, [Mg/Fe] has the most significant correlation with the IMF, while the relation between $\log(\alpha_{\text{IMF}})$ and [Fe/H] or $\log(\sigma)$ is mild. However, we recall from § 2.2 that there is some suspicious differences in [Fe/H] between the two samples. Until we have a sample covering the full range in σ and analyzed in a uniform manner, we note this caveat in the [Fe/H] and [Z/H] correlations with α_{IMF} .

To study the correlation between α_{IMF} and $\log(M_*)$, $\log(L_r)$ and $\log(M_{\text{dyn}})$, we further combine our sample with the galaxies that overlap between CvD and Cappellari et al. (2013a). Specifically, we make use of the stellar mass, dynamical mass, and luminosity measurements in Cappellari et al. (2013a). In the combined sample, $\log(M_*)$, $\log(L_r)$ and $\log(M_{\text{dyn}})$ all have moderate positive correlations with $\log(\alpha_{\text{IMF}})$. The

TABLE 2
PEARSON CORRELATION COEFFICIENTS FOR MASSIVE DATA

	[Fe/H]	[Mg/Fe]	[Z/H]	log(age) [Gyr]	log(M/L_r) [M_\odot/L_\odot]	log(α_{IMF})
log(σ/kms^{-1})	-0.13±0.17	0.44±0.11**	0.22±0.13	0.38±0.14*	0.40±0.13**	0.08±0.16
log(σ_c/kms^{-1})	-0.09±0.18	0.39±0.12*	0.22±0.14	0.32±0.15*	0.37±0.16*	0.14±0.17
log(σ_e/kms^{-1})	0.12±0.22	0.22±0.19	0.31±0.12*	0.03±0.25	0.25±0.14	0.18±0.19
log(M_*/M_\odot)	-0.30±0.14	-0.04±0.14	-0.35±0.12*	0.39±0.17**	0.35±0.19*	0.17±0.17
log(M_{dyn}/M_\odot)	-0.34±0.15*	0.03±0.17	-0.33±0.14*	0.35±0.14*	-0.05±0.23	-0.20±0.17
log(M_h/M_\odot)	-0.41±0.16*	0.25±0.17	-0.24±0.17	0.34±0.19*	0.12±0.25	-0.02±0.22
log(L_r/L_\odot)	-0.10±0.15	-0.23±0.12	-0.29±0.14	0.03±0.13	-0.21±0.14	-0.21±0.15
log(ν_{10})	-0.36±0.12*	0.23±0.15	-0.20±0.14	0.24±0.11	-0.01±0.15	-0.16±0.15
log($1 + \delta_g$)	-0.21±0.15	0.17±0.16	-0.09±0.17	0.05±0.12	-0.10±0.13	-0.14±0.15
log($\Sigma_{\text{Kroupa}}/(M_\odot \text{kpc}^{-2})$)	0.34±0.17*	0.12±0.17	0.46±0.12**	-0.17±0.13	0.28±0.16	0.34±0.14*
log(R_e/kpc)	-0.37±0.16*	-0.08±0.18	-0.47±0.12**	0.27±0.13	-0.15±0.20	-0.25±0.16

** Correlation is significant at the 0.01 level

* Correlation is significant at the 0.05 level

correlation coefficients are $r = 0.50 \pm 0.08$, 0.40 ± 0.09 and 0.42 ± 0.09 , respectively. Over the wide dynamic range afforded by the combined sample, we confirm that in general the IMF in more massive galaxies is more bottom heavy.

We next address whether the correlation between the IMF parameters and metallicity or [Mg/Fe] are driven by galaxy central velocity dispersion. The partial correlations at fixed log(σ) are shown in the rightmost column of Table 3, suggesting that both [Z/H] and [Mg/Fe] are moderately correlated with log(α_{IMF}) when the effect of σ is fixed. Therefore, although the correlation between galaxy central velocity dispersion and stellar population plays a role here, these moderate correlations with [Mg/Fe] and [Z/H] suggest that [Mg/Fe] and total metallicity are both driving IMF variation in a way that is independent of the effect from galaxy central velocity dispersion.

TABLE 3

	log(M/L_r)	log(α_{IMF})	log(α_{IMF})
MASSIVE			
[Fe/H]	-0.17±0.21	0.24±0.17	0.26±0.15
[Mg/Fe]	0.32±0.14*	0.00±0.16	-0.05±0.16
log(σ/kms^{-1})	0.41±0.13**	0.08±0.16	–
[Z/H]	0.08±0.20	0.25±0.17	0.25±0.15
[O/Fe]	0.19±0.12	-0.05±0.15	-0.09±0.16
[Na/Fe]	0.36±0.12*	0.25±0.16	0.23±0.15
[Ca/Fe]	0.19±0.14	0.01±0.13	-0.03±0.16
[Ti/Fe]	-0.12±0.16	-0.19±0.15	-0.21±0.15
log($\Sigma_{\text{Kroupa}}/(M_\odot \text{kpc}^{-2})$)	0.29±0.16	0.34±0.15*	0.36±0.15*
MASSIVE+CvD			
[Fe/H]	0.18±0.11	0.31±0.10**	0.15±0.11
[Mg/Fe]	0.73±0.06**	0.66±0.08**	0.44±0.09**
log(σ/kms^{-1})	0.69±0.06**	0.56±0.07**	–
[Z/H]	0.49±0.09**	0.56±0.08**	0.32±0.10**

NOTE. — Pearson Correlation Coefficients (left) and Partial Correlation Coefficients, controlling log(σ) (right) for MASSIVE data (top), and the combined sample MASSIVE+CvD (bottom)

** Correlation is significant at the 0.01 level

* Correlation is significant at the 0.05 level

In summary, by complementing our sample with lower masses galaxies in CvD and (Cappellari et al. 2013a), we find that the IMF of ETGs becomes increasingly bottom heavy with increasing central velocity dispersion, luminosity, stellar mass, and dynamical mass. [Mg/Fe] and [Z/H] are positively correlated with the IMF and these trends are not driven by their relation to the galaxy central velocity dispersion.

TABLE 4
BEST-FIT PARAMETERS

Eq (1)	c_0	c_1	c_2
MASSIVE	0. - 1 ± 0.87	0.10 ± 0.38	-0.04 ± 0.46
CvD	-0.36 ± 0.34	0.03 ± 0.16	1.91 ± 0.33
MASSIVE+CvD	-0.66 ± 0.34	0.24 ± 0.16	1.10 ± 0.26
Eq (2)	c_0	c_1	c_2
MASSIVE	0.07 ± 0.78	-0.01 ± 0.33	0.69 ± 0.37
CvD	-1.25 ± 0.43	0.57 ± 0.19	0.45 ± 0.43
MASSIVE+CvD	-1.02 ± 0.34	0.47 ± 0.15	0.37 ± 0.13

Eq (1): log(α_{IMF}) = $c_0 + c_1(\log \sigma) + c_2([\text{Mg}/\text{Fe}]$)

Eq (2): log(α_{IMF}) = $c_0 + c_1(\log \sigma) + c_2([\text{Z}/\text{H}]$)

4.5. Multivariate Linear Regression

We have presented the correlations between stellar populations, IMF parameters, and galaxy dynamical properties. We find that the effective velocity dispersion (σ), [Mg/Fe], [Z/H] and possibly the effective stellar mass surface density (Σ_{Kroupa}), are all correlated with α_{IMF} . Now we examine the relative strength of these correlations by fixing the effects of certain variables. Following the analysis by Smith (2014), we first focus on σ and [Mg/Fe], since they are shown to be strongly correlated with α_{IMF} in the combined sample. We perform a bi-variate linear regression of log(σ), [Mg/Fe] and log(α_{IMF}) in three datasets: our sample alone, the CvD alone, and the combined sample. Variables are standardized prior to the fitting. In the equation

$$\log(\alpha_{\text{IMF}}) = c_0 + c_1(\log \sigma) + c_2([\text{Mg}/\text{Fe}]) \quad (1)$$

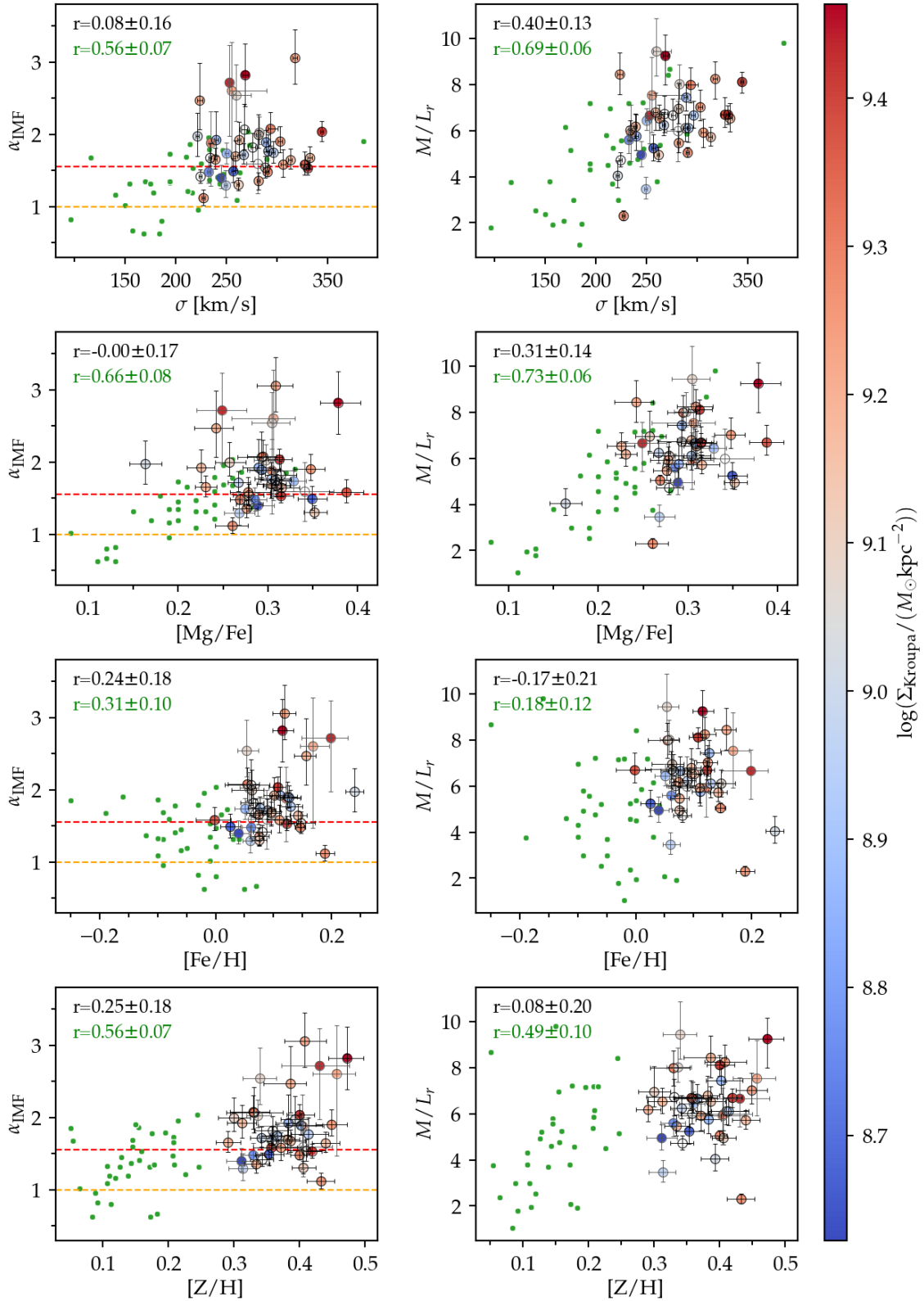


FIG. 8.— From top to bottom: M/L_r and the IMF α -mismatch parameter as a function of σ , [Mg/Fe], [Fe/H] and estimated total metallicity [Z/H]. Red and orange horizontal lines indicate Salpeter and Kroupa IMF. Pearson correlation coefficients and its 1σ uncertainty are shown in our sample alone (black), and in the combined sample (green). The strong correlation between [Mg/Fe] and IMF suggest that the star formation timescale may play an important role in shaping the stellar IMF.

The best-fit parameters fits to all three samples are shown in Table 4.

Based on the combined sample, the best-fit parameters suggest that [Mg/Fe] plays a more important role in driving the variation of α_{IMF} than σ . The dominant role of [Mg/Fe] using a bi-variate model of the combined sample is consistent with CvD and Smith (2014). It suggests that [Mg/Fe] is the more important driver for $\log(\alpha_{\text{IMF}})$ when considering both galaxy central velocity dispersion and [Mg/Fe] based on stellar population synthesis. However within our sample, these two variables alone hardly describe the variance of $\log(\alpha_{\text{IMF}})$, indicating that other variables must also be considered.

Based on the strong correlation between IMF and metallicity within our sample and in the combined sample, we further test the bi-variate linear regression with $\log(\alpha_{\text{IMF}})$ as the dependent variable using $\log(\sigma)$ and [Z/H] as independent variables using the following equation

$$\log(\alpha_{\text{IMF}}) = c_0 + c_1(\log \sigma) + c_2([\text{Z}/\text{H}]) \quad (2)$$

The results from the combined sample suggest that total metallicity and $\log(\sigma)$ are of similar importance in driving the IMF variation. We will discuss the physical implications in § 6. As discussed in § 4.3, Σ is also an important property for the IMF and may be a driver of IMF variations at the high mass end. However, in this work we do not include Σ in the discussion since it is sensitive to the consistency in the measurements of luminosity and R_e .

4.6. Environment

In Table 2 we also present [Fe/H], [Mg/Fe] and the IMF α -mismatch parameter as a function of three environment indicators: logarithmic halo mass (M_h), local over-density (ν_{10}) and large-scale galaxy density ($1 + \delta_g$) (Veale et al. 2017b). ν_{10} represents the luminosity density of galaxies in a sphere enclosing the 10th nearest neighbour, and δ_g represents the luminosity-weighted galaxy density contrast with a smoothing scale of 5.7 Mpc.

There is no significant correlation between α_{IMF} and any environmental indicator within our sample. This is consistent with what was found in Rosani et al. (2018). However, we do find a negative correlation between [Fe/H] and the logarithmic dynamical mass within our sample, which is not consistent with the significant positive correlation found in the combined sample where $r_{[\text{Fe}/\text{H}]-\log(M_{\text{dyn}})} = 0.48$, $p = 2.7 \times 10^{-5}$, i.e., over a large dynamic range the massive ETGs in our sample are still found to be more metal rich compared to lower mass ETGs. We note that the negative correlation within our sample may be at least partially due to differences in R_e measurements, as [Fe/H] is sensitive to the choices of apertures. In an upcoming paper, we will study the local variations in stellar population parameters, the IMF, and their relations with environmental indicator.

With the large dynamical range in the combined sample, [Mg/Fe] seems to be an important parameter for the IMF. In upcoming work, we will expand our investigation to larger radii where galaxy properties are dominated by accretion and could be more sensitive to the environment. We will study the relation between local IMF or IMF gradient with [Mg/Fe] and explore any connection with the environment.

5. DYNAMICAL VERSUS STELLAR MASSES

While independent modeling techniques from stellar population synthesis and dynamical modeling both reveal similar

global IMF trends. The concerning aspect arises when comparing the IMF constraints from different methods, because the inferred M/L are not consistent on a galaxy-by-galaxy basis (e.g. Smith 2014; Newman et al. 2017). Smith (2014) compare the stellar M/L in the overlap sample between Conroy & van Dokkum (2012b) and Cappellari et al. (2013a), and conclude that there is no significant correlation between the stellar M/L or IMF mismatch parameter inferred by the two studies. Smith (2014) mention that M/L and α_{IMF} variations within galaxies could lead to discrepancies due to the different apertures used for the dynamical and stellar population synthesis studies.

At the very least, the stellar-population-based masses should not violate the mass budget. Here we compare the stellar M/L with the estimated total M_{dyn}/L_r to ensure that our inferred stellar masses are physical. As described in § 4, we estimate the stellar M/L within R_e with a linear extrapolation of $\log R - \log(M/L)_r$. Since the dynamical measurements are done within R_e , it is important to account for the M/L variation within galaxies. Most galaxies in our sample have a declining radial profile of M/L , and on average the ratio between central M/L and extrapolated M/L within R_e is 1.3. We compare our results with recent literature in Figure 9 and present the main result in this section in Figure 9(d).

In Figure 9(a), we compare the stellar M/L with several measurements in the literature. It shows the stellar M/L_r in galaxy centers as a function of luminosity weighted velocity dispersion within R_e . Black data points show our results where the M/L is measured within $R_e/8$. Orange data points show the M/L_r of the stellar components within a sphere of radius $r \sim R_e$ from Cappellari et al. (2013a), where the results were from the best-fitting JAM model with an assumption of NFW halo for the dark matter components. Green data points show the M/L_r from full spectral modeling within a radius of $R_e/8$ from CvD. Blue data points show results from Newman et al. (2017). The M/L of the three galaxies are constrained by lensing and within an aperture of $2.2''$ (1.4-2.2kpc), with the dark matter contribution estimated from the EAGLE simulations. Note that unlike all other data points in the sample, the velocity dispersions of these three galaxies are measured in an aperture of $R_e/2$. There seems to be an offset between our results and the three galaxies from Newman et al. (2017). The apertures correspond to 0.2 to $0.7 \times R_e$ and are all larger than $R_e/8$ in our sample. If α_{IMF} declines with radius, then putting the galaxies in our sample with $R_e/8$ apertures on the same scale as the three galaxies from Newman et al. (2017) may lower the α_{IMF} , and could possibly make the two sets of data in better agreement.

Figure 9(b) shows the dynamical M/L_r as a function of σ_e . Our results are compared with Cappellari et al. (2013a) (orange data points) whose measurements come from the best-fitting self-consistent JAM model. As described in § 4, we use an empirical relation from Cappellari et al. (2006) to estimate M_{dyn} . The correlation is confirmed by Cappellari et al. (2013a). There is an apparent offset in the overlapping σ_e region. There are likely many factors contributing to this apparent offset. Our photometry is based on deeper imaging, and our R_e measurements may be systematically different as well. Furthermore, our sample is dominated by slow rotators, which perhaps requires a different virial factor β . With the empirical relation from Cappellari et al. (2006), Figure 9(b) suggests that we may systematically underestimate the dynamical mass of our galaxies compared to galaxies with sim-

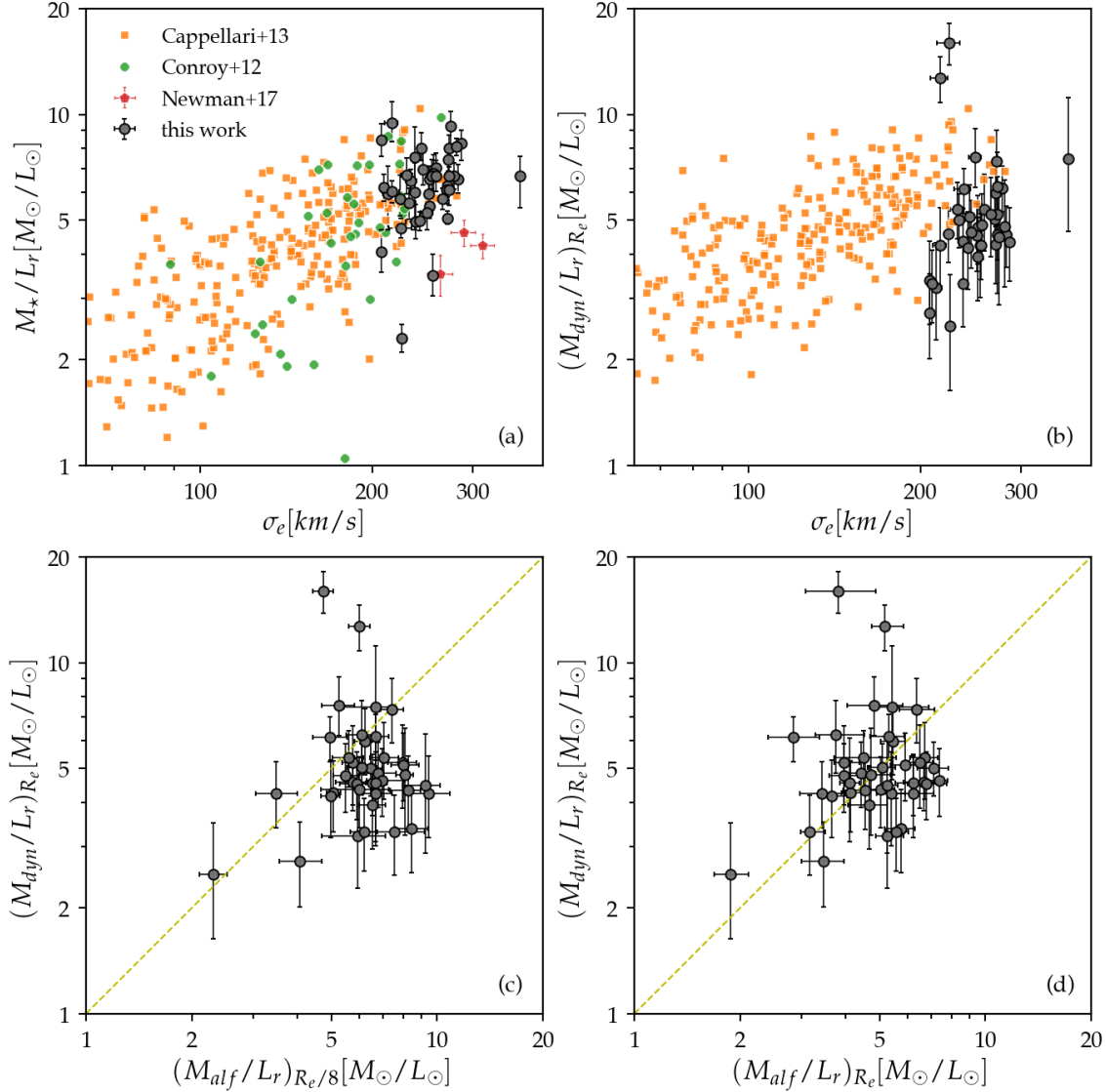


FIG. 9.— Panel (a): r -band stellar M/L in galaxy centers as a function of σ_e . Results from this work (black) are compared to the estimated stellar population M/L in A3D (orange dots), in Newman et al. (2017) (blue) and in CvD (green). Panel (b): Dynamical M/L in r -band as a function of σ_e . Note that the stellar M/L are derived in the aperture of $R_e/8$, and the dynamical M/L indicate an average value within R_e . Yellow dashed and dotted lines indicates 1:1 comparisons. Panel (c): Comparison between the M/L from a1f and the estimated dynamical M/L . Panel (d): M_{dyn}/L_r are extrapolated to an aperture of R_e . The majority galaxies in our sample are consistent with M_{dyn}/L_r estimation within 1σ uncertainty.

ilar σ_e in ATLAS^{3D}. We consider several possibilities that could mitigate the difference: First, the luminosity and structural measurements both matter. For the galaxies with both SDSS and Siena photometry, if we use the size and luminosity from SDSS `cmodel`, the M_{dyn}/L would increase by $\sim 14\%$, suggesting that both the R_e measurement and the depth affect the M_{dyn}/L measurement. Considering that galaxies in our sample have extended stellar structures, deep photometry is crucial to determine the sky background level and light profiles, therefore we choose to adopt the Siena photometry described in § 2 where available. Second, the mean dynamical M/L_r in our sample is $\langle M_{dyn}/L_r \rangle = 5.3 \pm 2.4 M_\odot/L_{r,\odot}$. If we use $\beta = 4$ from Wolf et al. (2010), the mean dynamical M/L_r will increase by 60%. Currently we do not have more accurate dynamical mass measurements and do not have better galaxy-by-galaxy constraints on β , therefore we adopt $\beta = 2.5$ from A3D. In the future we will work on an updated calibration of the relation for virial mass estimation

based on detailed dynamical modeling of ETGs in our sample. New results from Jeans Anisotropic models (Cappellari 2008) or Schwarzschild orbit superposition models (Schwarzschild 1979; Thomas et al. 2016) may help alleviate the discrepancy.

From Figure 9(a), our results of M_*/L are consistent with CvD and A3D in the regime of σ_e from 220 to 300 km s^{-1} and indicate galaxies in this regime are better described by a bottom heavy IMF. In Figure 9(c) we compare the dynamical mass-to-light ratio (M_{dyn}/L) within R_e with M_*/L measured directly within $R_e/8$: Most galaxies (31 out of 39) in our sample have a dynamical M/L_r that is smaller than the stellar M/L_r within $R_e/8$, therefore it seems there’s an apparent disagreement and violation of mass budget if we do not use consistent apertures. However, this is partly due to the variation of M/L within galaxies. In Figure 9(d), we further compare the dynamical M/L_r within R_e to the extrapolated stellar M/L_r (§ 4.1) within R_e . The mean M_{dyn}/L and M_*/L within R_e are $5.3 \pm 2.4 M_\odot/L_\odot$ and $5.0 \pm 1.2 M_\odot/L_\odot$, respectively,

and are both smaller compared to the mean central M_*/L of $6.4 \pm 1.4 M_\odot/L_\odot$. If we use a consistent aperture of R_e , most galaxies in our sample have M_*/L_r smaller than the M_{dyn}/L_r (20 out of 39), and most galaxies have consistent M_*/L_r and M_{dyn}/L_r within $1-\sigma$ uncertainty (30 out of 39). Our result suggests that overall our stellar M/L_r constraints are within the mass budget. Figure 9 highlights the importance of using consistent apertures when comparing different works.

6. DISCUSSION

We have presented the correlations between stellar populations, IMF and galaxy dynamical properties in § 4. In § 6.1 we discuss the physical implication. In § 6.2 we compare our fiducial model with the 2pl IMF model where the low cutoff is fixed to $0.08M_\odot$.

6.1. Physical Implications

By combining our sample with low mass galaxies in § 4.4 we present positive correlations between $\log(\alpha_{\text{IMF}})$ and σ , $\log(M_*)$, $\log(L_r)$ and $\log(M_{\text{dyn}})$, and confirm the trend towards an increasing α_{IMF} in more massive systems found in prior work (e.g. Conroy & van Dokkum 2012b; Cappellari et al. 2013a; Spiniello et al. 2011; Treu 2010; La Barbera et al. 2013), i.e., the IMF in ETG centers becomes increasingly bottom heavy with increasing galaxy masses. In addition, we have found that $\log(\alpha_{\text{IMF}})$ is moderately correlated with $\log(\Sigma_{\text{Kroupa}})$ within our sample (§ 4.3), and also moderately correlated with $[\text{Mg}/\text{Fe}]$ and total metallicity $[\text{Z}/\text{H}]$ in the combined sample (§ 4.4). In this section, we compare our results with previous literature and discuss the physical implications.

There has been a lot of debate on the physical drivers of IMF variation. Many recent observations reveal a correlation between IMF and galaxy stellar metallicity (e.g. Martín-Navarro et al. 2015; Zhou et al. 2019; van Dokkum et al. 2017; Parikh et al. 2018). On the other hand, CvD reported a correlation between α_{IMF} and both σ and $[\text{Mg}/\text{Fe}]$, but only a mild correlation with total metallicity. Also some dynamical analysis suggest no significant correlation with metallicity or $[\text{Mg}/\text{Fe}]$ (e.g. McDermid et al. 2014; Li et al. 2017). There is not yet a clear conclusion on this topic. One difference between our results and many previous studies is that we find clear evidence that *both* the central metallicity and $[\text{Mg}/\text{Fe}]$ are positively correlated with the IMF. In the combined sample, among all the parameters, $[\text{Mg}/\text{Fe}]$ is the one that has the strongest correlation with α_{IMF} . As shown in Figure 8, the $[\text{Mg}/\text{Fe}]$ in our sample is on average higher than the lower mass galaxies in CvD. If we use $[\text{Mg}/\text{Fe}]$ to trace the α -abundance and use it as an indicator of the past star formation timescale (e.g. Thomas et al. 2005), the average $\langle [\text{Mg}/\text{Fe}] \rangle = 0.29 \pm 0.04$ suggests that in the centers ($R_e/8$) of the massive ETGs in our sample, the average star formation timescale is only $\Delta t \sim 250$ Myr, inferring an average star formation rate surface density ($M_*/(4\pi R^2 \Delta t)$) of $117 M_\odot \text{yr}^{-1} \text{kpc}^{-2}$. Based on these estimates, the stars in the central region of these ETGs are formed in extreme environments through a starburst (e.g. Kennicutt & Evans 2012; Bouche et al. 2007; Daddi et al. 2010).

The $\log(\Sigma) - [\text{Fe}/\text{H}]$ and $\log(\Sigma) - [\text{Z}/\text{H}]$ correlations (§ 4.3, Table 2) within our sample are also important, as both metallicity and stellar surface density are positively correlated with $\log(\alpha_{\text{IMF}})$. Within our sample, the metallicity has a significant positive correlation with the stellar surface density and a mild

negative correlation with logarithmic stellar mass (Table 2). Our finding is consistent with the picture that higher density ETGs retain more of their metals and are less likely to be disrupted (e.g. Barone et al. 2018). The connection between the IMF and galaxy stellar metallicity has been shown in prior work both from observations (e.g. Martín-Navarro et al. 2015; Zhou et al. 2019; van Dokkum et al. 2017; Parikh et al. 2018), and simulations (e.g. Sharda & Krumholz 2021; Chon et al. 2021). For example, Sharda & Krumholz (2021) studied the characteristic mass in collapsing dusty gas clouds and found that high pressure ISM and high metallicity will result in low characteristic mass and therefore explained the bottom-heavy IMF found in massive ETGs. Since the high surface density suggests high gas pressure when the stars are formed, the simulation result is supported by our data and explains that the metallicity and stellar surface density are driving the IMF variation in different ways.

The connection between galaxy compactness and the stellar IMF has also been suggested in several recent papers (e.g. Chabrier et al. 2014; La Barbera et al. 2019; Smith et al. 2015; Barbosa et al. 2021; van Dokkum et al. 2017). Martín-Navarro et al. (2015) measured the IMF of a massive relic galaxy, NGC 1277 (Trujillo et al. 2014), and found that it is bottom heavy at all radii. Villaume et al. (2017) studied various compact stellar systems, and found that despite their large metallicity and $[\text{Fe}/\text{H}]$ range, they all have elevated α_{IMF} with low scatter. All of these works indicate the trend that more compact galaxies are more likely to have bottom heavier IMF.

What may be the physical explanation? First of all, simulations (e.g. Chabrier et al. 2014) reveal that star formation in the extreme environment of very dense and turbulent gas will extend the peak mass of the IMF to lower masses. Compared to massive spiral galaxies or less compact massive ETGs, the extreme local environment in the most massive compact ETGs could be the reason for their bottom heavy IMF. Second, many simulations and observations support the two-phase formation scenario for massive ETGs (e.g. Oser et al. 2010; van Dokkum et al. 2010; Patel et al. 2013). The idea is that local massive ETGs first formed as compact “red nuggets” at high redshift due to strong dissipational processes. At later times, they experienced the accretion of lower-mass systems. As a result, they build up their effective radii over time. Compactness therefore tracks the relative fraction of the stars formed in the first phase (e.g. Bezanson et al. 2009). The compact galaxies in our sample may preserve more of the properties of the ‘first phase’ formation at high redshift and have been less disturbed by the minor mergers at low redshifts. For the less compact galaxies the stellar IMF is affected by both in-situ and ex-situ activity. Our results are consistent with the picture that both the formation time and the star formation timescale are related to the stellar IMF in the galaxy centers.

Our next step is to study the local IMF of massive ETGs as a function of radius. Previous studies have revealed steep gradients in the metallicity profile with radius, and in general a nearly flat $[\text{Mg}/\text{Fe}]$ radial profile in massive ETGs. The latter could be due to the environmental quenching of low-mass galaxies, which were accreted and distributed at the outskirts of massive galaxies (e.g. Gu et al. 2018; Gu et al. 2020). Due to the differences in the gradients, we expect to see a radial dependence from the relations among metallicity, $[\text{Mg}/\text{Fe}]$, and IMF. In the next paper we will focus on their relations at different fractions of R_e . How the correlations hold at different radii will help us understand which of the stellar population

properties are fundamental, and the role of in-situ and ex-situ processes in driving IMF variation.

Our current work is limited by the dynamic range in stellar mass of the MASSIVE sample. Although we include low mass galaxies from CvD in our analysis, the stellar populations studied are restricted to total metallicity and $[\text{Mg}/\text{Fe}]$. § 4.2 shows the trend that $[\text{Na}/\text{Fe}]$ and $[\text{O}/\text{Fe}]$ both increase with increasing central velocity dispersion (Figure 6). In the future, through studying low mass ETGs with a consistent model we will be able to tell whether other elemental abundances are related to IMF variations.

6.2. IMF Model Comparison

As indicated by Newman et al. (2017), the parameterizations of IMF models are important in spectral modeling, and different functional forms (e.g., single or double slopes, with or without a low-mass cutoff) of the IMF may lead to different inferred M/L . As described in § 2, our fiducial IMF model has a slope above $1M_{\odot}$ fixed to 2.3, and free parameters imf1 and imf2 for the slopes below and above $0.5M_{\odot}$. In addition, imf3 is used to describe the cutoff mass at the low mass end. In this section, we test the results of different IMF parameterizations by comparing our results to the assumption that the IMF has the form of a double power-law with a fixed cutoff mass at $0.08M_{\odot}$, the canonical hydrogen-burning limit.

We compare results from these two models in Figure 10. In the left panels, we compare the median (error-bars indicate the 16th and 84 percentiles) of the posteriors of α_{IMF} (top), and the slope in the intermediate mass range (imf2) (bottom). The y-axis represents results from the model with fixed cutoff mass, and those on the x-axis represent our fiducial model. In general they are consistent with each other. The average ratio of M/L_r and α_{IMF} is 11% higher in the double power-law model than our fiducial model with very little scatter. In general the fixed low cutoff mass result in slightly higher M/L , indicating that our results do not depend heavily on the choice of the IMF functional form. Adopting the IMF model with fixed cutoff mass will not alter our conclusions about the global trend that the IMF in ETG centers becomes more bottom heavy with increasing stellar mass. As shown in Figure 10(b) the slopes in the intermediate mass range are consistent with each other, suggesting that the intermediate mass slope is not very sensitive to the IMF form.

Figure 10(c) shows the low-mass IMF slope, imf1 , in our fiducial model (black) and the model with fixed cutoff mass (red) as a function of α_{IMF} . Panel (d) shows cutoff mass in our fiducial model as a function of α_{IMF} . There is apparently some degeneracy between the low mass slope $< 0.5M_{\odot}$ imf1 and the low mass cutoff imf3 . By allowing imf3 to vary, we estimate that $\langle \text{imf3} \rangle = 0.16 \pm 0.05M_{\odot}$. As indicated by the Pearson correlation coefficient at the lower right corners, imf1 is moderately positively correlated with α_{IMF} , and imf3 is negatively correlated with α_{IMF} , which makes sense since allowing the low cutoff mass to vary will result in decreasing M/L with increasing cutoff mass. On the other hand if we fix imf3 (panel (c), red), α_{IMF} primarily depends on imf1 with a correlation coefficient of 0.64. imf2 is stable (panel (d)) with and without a flexible low cutoff mass, suggesting that a free intermediate mass slope is necessary in the IMF model, and a double power-law IMF form is a better choice than a single power law. For high S/N galaxies the estimated low-mass cut-off values, imf3 , are still larger than $0.08M_{\odot}$, suggesting that imf3 is also a useful free parameter in describing the IMF at low mass range. However, we do not

intend to use this as an accurate measurement of the cutoff mass. We simply use imf3 as an additional free parameter, since a fixed $0.08M_{\odot}$ does not apply for all galaxies and may over-estimate the M/L and α_{IMF} . If we switch our results to the $2pl$ model, the positive correlations between $\log(\alpha_{\text{IMF}})$ and $[\text{Mg}/\text{Fe}]$, $[\text{Z}/\text{H}]$, $\log(\sigma)$ are still strongly held, although the $\log(\Sigma_{\text{Kroupa}}) - \log(\alpha_{\text{IMF}})$ within our sample becomes less significant with $r = 0.27 \pm 0.16$

7. SUMMARY

We have conducted detailed full spectral modeling on a sample of 41 massive early-type galaxies in the volume-limited MASSIVE survey to constrain their stellar populations and the stellar initial mass function. Galaxies in our sample are among the most massive in the universe. We extract spectra observed by LDSS-3 on the Magellan/Clay telescope, using an effective circular aperture of $R_e/8$. We obtain high S/N spectra with $\langle S/N \rangle = 234 \text{ \AA}^{-1}$ in $0.8 - 0.9 \mu\text{m}$, and fit for stellar population parameters, M/L and IMF mismatch parameter, α_{IMF} . Our main results are summarized as follows:

1. In our default model, the stellar IMF is described by three free parameters: the low and intermediate mass slopes, and a low mass cutoff. Spectral modeling using an IMF fixed to Kroupa results in visibly worse residuals and fails to describe the spectra in the centers of massive early-type galaxies.
2. Within $R_e/8$, the IMF of all galaxies in our sample are more bottom heavy than Kroupa. The α_{IMF} mismatch parameter of the whole sample is $\langle \alpha_{\text{IMF}} \rangle = \langle (M/L)/(M/L)_{\text{MW}} \rangle = 1.84 \pm 0.43$. On average these massive galaxies have stellar IMF bottom heavier than the IMF with a Salpeter slope.
3. Combining the results of galaxies in our sample with lower-mass ETGs in the previous literature, we confirm the positive trend that the central IMF becomes bottom heavier with increasing galaxy central velocity dispersion, stellar mass, luminosity and dynamical mass (§ 4.4). We find correlations between $\log(\alpha_{\text{IMF}})$ and, $\log(\sigma)$, $[\text{Mg}/\text{Fe}]$, and total metallicity ($[\text{Z}/\text{H}]$) (§ 4.4). Within our sample, $\log(\alpha_{\text{IMF}})$ is positively correlated with both the effective surface mass density (Σ) and total metallicity (§ 4.3), suggesting that galaxy compactness might be an important property related to IMF variation.
4. We estimate the dynamical masses and compare them with the stellar mass within R_e . Most of the galaxies have stellar mass consistent within 1σ uncertainty with the estimated dynamical mass (§ 5). Most galaxies have central M/L within $R_e/8$ higher than the average dynamical M/L within R_e , and thus choice of apertures is important in the comparison.
5. The compact galaxies in our sample may preserve more of the properties from their 'first phase' of formation. Our results are consistent with the picture that both the formation time and the star formation timescale are related to the stellar IMF in the galaxy centers.

In an upcoming paper, we will look into the radial dependence of the IMF and stellar populations, and study the connections between these local properties. This is important

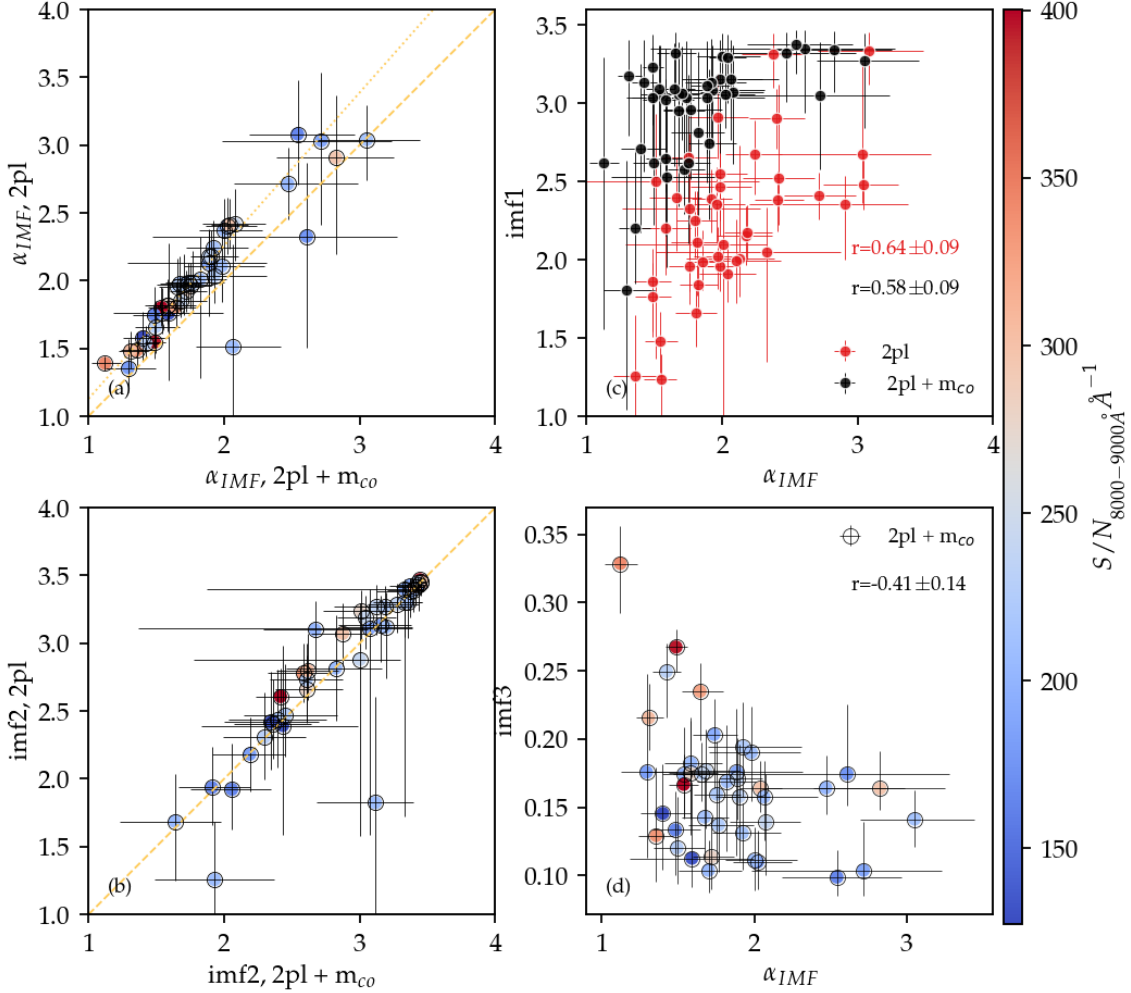


FIG. 10.— Comparison of IMF parameters from two assumptions of IMF model: (1) double power-law with a fixed low-mass cutoff of $0.08M_{\odot}$, and (2) double power-law with variable low-mass cutoff (fiducial model in this work). imf1 and imf2 are the low and intermediate mass IMF slopes, respectively, while imf3 is the low mass cutoff. (a) and (b): comparison of α_{IMF} and imf2 between the two models: they are overall consistent, but the M/L_r in the double power-law model is 12% higher in M/L_r compared to our fiducial model (orange dotted line). (c) and (d): imf1 and imf3 as a function of α_{IMF} , and the corresponding Pearson correlation coefficients.

since we know there are usually strong gradient in metallicity, and the radial variation of population properties such as α -abundances and stellar age might be sensitive to the large scale environment. In the future, a larger sample of lower mass galaxies will help with the investigation of the physical mechanisms driving IMF variations over a larger dynamical range, and hopefully will provides us insights on any connections between galaxy stellar IMF with properties other than $[\text{Mg}/\text{Fe}]$ and $[\text{Z}/\text{H}]$. A large sample of lower mass ETGs including both compact and diffuse ETGs will help verify how significant and on what scale galaxy compactness is related to galaxy IMF.

This paper includes data gathered with the 6.5 meter Magellan Telescopes located at Las Campanas Observatory, Chile. The authors are pleased to acknowledge that the work reported on in this paper was substantially performed using the Princeton Research Computing resources at Princeton University which is consortium of groups led by the Princeton Institute for Computational Science and Engineering (PICSciE) and Office of Information Technology’s Research Computing. This project used data obtained with the Dark Energy Cam-

era (DECam), which was constructed by the Dark Energy Survey (DES) collaboration. Funding for the DES Projects has been provided by the U.S. Department of Energy, the U.S. National Science Foundation, the Ministry of Science and Education of Spain, the Science and Technology Facilities Council of the United Kingdom, the Higher Education Funding Council for England, the National Center for Supercomputing Applications at the University of Illinois at Urbana-Champaign, the Kavli Institute of Cosmological Physics at the University of Chicago, Center for Cosmology and Astrophysics at the Ohio State University, the Mitchell Institute for Fundamental Physics and Astronomy at Texas A&M University, Financiadora de Estudos e Projetos, Fundacao Carlos Chagas Filho de Amparo, Financiadora de Estudos e Projetos, Fundacao Carlos Chagas Filho de Amparo a Pesquisa do Estado do Rio de Janeiro, Conselho Nacional de Desenvolvimento Cientifico e Tecnologico and the Ministerio da Ciencia, Tecnologia e Inovacao, the Deutsche Forschungsgemeinschaft and the Collaborating Institutions in the Dark Energy Survey. The Collaborating Institutions are Argonne National Laboratory, the University of California at Santa Cruz, the University of Cambridge, Centro de In-

vestigaciones Energeticas, Medioambientales y Tecnologicas-Madrid, the University of Chicago, University College London, the DES-Brazil Consortium, the University of Edinburgh, the Eidgenossische Technische Hochschule (ETH) Zurich, Fermi National Accelerator Laboratory, the University of Illinois at Urbana-Champaign, the Institut de Ciencies de l'Espai (IEEC/CSIC), the Institut de Fisica d'Altes Energies, Lawrence Berkeley National Laboratory, the Lud-

wig Maximilians Universitat Munchen and the associated Excellence Cluster Universe, the University of Michigan, NSF's NOIRLab, the University of Nottingham, the Ohio State University, the University of Pennsylvania, the University of Portsmouth, SLAC National Accelerator Laboratory, Stanford University, the University of Sussex, and Texas A&M University.

APPENDIX

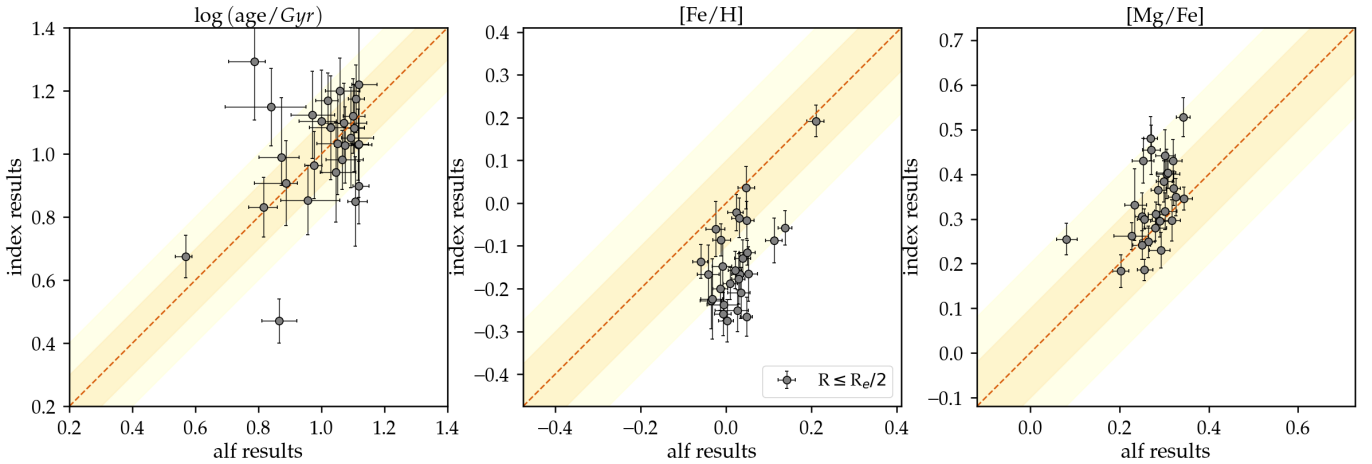


FIG. 11.— Comparison between full spectral modeling results from `alf` in this work, and results from Lick indices measured on IFS data. Orange and yellow regions indicate a difference of 0.1 dex and 0.2 dex, respectively.

In this section we compare the stellar populations: stellar age, $[\text{Fe}/\text{H}]$ and $[\text{Mg}/\text{Fe}]$ in 28 ETGs in this work and [Greene et al. 2019](#) (MASSIVE Paper XII). The stellar populations in MASSIVE Paper XII are measured with Lick indices on spectra observed with the Mitchell IFS at the McDonald Observatory. The wavelength ranges in indices measurement is 3650–5850Å. In the comparison, we use a consistent aperture of $R_e/2$, where R_e are measured on CFHT K -band imaging (Quenneville in prep). The results are shown in Figure 11. The index results are the mean stellar populations within $R_e/2$, while the `alf` results are derived modeling a stacked spectra within an effective circular aperture of $R_e/2$. On average, the offsets are $\langle [\text{Fe}/\text{H}]_{\text{index}} \rangle - \langle [\text{Fe}/\text{H}]_{\text{alf}} \rangle = -0.16$ dex, $\langle \log(\text{age}/\text{Gyr})_{\text{index}} \rangle - \langle \log(\text{age}/\text{Gyr})_{\text{alf}} \rangle = 0.015$ dex and $\langle [\text{Mg}/\text{Fe}]_{\text{index}} \rangle - \langle [\text{Mg}/\text{Fe}]_{\text{alf}} \rangle = 0.06$ dex. The overall agreement is encouraging. On average the $[\text{Fe}/\text{H}]$ in our results is higher than the index results from MASSIVE Paper XII. We note that in addition to the differences in model and modeling methods, there are differences in wavelength ranges, data quality, and spatial information in these two works.

REFERENCES

- Abolfathi, B., Aguado, D. S., Aguilar, G., et al. 2018, *ApJS*, 235, 42 [2.3](#)
 Bacon, R., Copin, Y., Monnet, G., et al. 2001, *MNRAS*, 326, 23 [2.2](#)
 Barbosa, C. E., Spiniello, C., Arnaboldi, M., et al. 2021, *A&A*, 645, L1 [1](#), [6.1](#)
 Barone, T. M., D’Eugenio, F., Colless, M., et al. 2018, *ApJ*, 856, 64 [6.1](#)
 Bastian, N., Covey, K. R., & Meyer, M. R. 2010, *ARA&A*, 48, 339 [1](#)
 Bezanson, R., van Dokkum, P. G., Tal, T., et al. 2009, *ApJ*, 697, 1290 [6.1](#)
 Bouche, N., Cresci, G., Davies, R., et al. 2007, *The Astrophysical Journal*, 671, 303 [6.1](#)
 Bundy, K., Bershady, M. A., Law, D. R., et al. 2015, *The Astrophysical Journal Letters*, 798, 7 [2.4](#)
 Cappellari, M. 2008, *MNRAS*, 390, 71 [5](#)
 Cappellari, M., Bacon, R., Bureau, M., et al. 2006, *MNRAS*, 366, 1126 [1](#), [4.1](#), [5](#)
 Cappellari, M., Emsellem, E., Krajnóvić, D., et al. 2011, *MNRAS*, 413, 813 [2.2](#)
 Cappellari, M., Scott, N., Alatalo, K., et al. 2013a, *MNRAS*, 432, 1709 [1](#), [2.2](#), [4.1](#), [4.4](#), [5](#), [6.1](#)
 Cappellari, M., McDermid, R. M., Alatalo, K., et al. 2013b, *MNRAS*, 432, 1862 [4.1](#), [4.2](#)
 Cenarro, A. J., Gorgas, J., Vazdekis, A., Cardiel, N., & Peletier, R. F. 2003, *MNRAS*, 339, L12 [1](#)
 Chabrier, G., Hennebelle, P., & Charlot, S. 2014, *ApJ*, 796, 75 [6.1](#)
 Choi, J., Dotter, A., Conroy, C., et al. 2016, *ApJ*, 823, 102 [3.1](#)
 Chon, S., Omukai, K., & Schneider, R. 2021, arXiv e-prints, arXiv:2103.04997 [6.1](#)
 Conroy, C., Graves, G. J., & van Dokkum, P. G. 2014, *The Astrophysical Journal Letters*, 780, 33 [3](#), [4.3](#)
 Conroy, C., & van Dokkum, P. 2012a, *The Astrophysical Journal Letters*, 747, 69 [1](#), [2.2](#), [3](#)
 Conroy, C., & van Dokkum, P. G. 2012b, *The Astrophysical Journal Letters*, 760, 71 [1](#), [4.2](#), [5](#), [6.1](#)
 Conroy, C., van Dokkum, P. G., & Villaume, A. 2017, *ApJ*, 837, 166 [1](#), [3.1](#)
 Conroy, C., Villaume, A., van Dokkum, P. G., & Lind, K. 2018, *ApJ*, 854, 139 [3](#)
 Daddi, E., Elbaz, D., Walter, F., et al. 2010, *The Astrophysical Journal*, 714, L118 [6.1](#)
 Davis, T. A., Greene, J., Ma, C.-P., et al. 2016, *MNRAS*, 455, 214 [2.2](#)
 Dutton, A. A., Mendel, J. T., & Simard, L. 2012, *MNRAS*, 422, L33 [1](#)
 Ene, I., Ma, C.-P., Walsh, J. L., et al. 2020, *ApJ*, 891, 65 [2.3](#)
 Ferreras, I., La Barbera, F., de La Rosa, I. G., et al. 2013, *MNRAS*, 429, L15 [1](#)
 Foreman-Mackey, D., Hogg, D. W., Lang, D., & Goodman, J. 2013, *Publications of the Astronomical Society of the Pacific*, 125, 306 [3.1](#)
 Graves, G. J., Faber, S. M., Schiavon, R. P., & Yan, R. 2007, *The Astrophysical Journal*, 671, 243 [4.3](#)

- Greene, J. E., Janish, R., Ma, C.-P., et al. 2015, *ApJ*, 807, 11 [4.3](#)
- Greene, J. E., Veale, M., Ma, C.-P., et al. 2019, *ApJ*, 874, 66 [7](#)
- Gu, M., Conroy, C., & Brammer, G. 2018, *The Astrophysical Journal Letters*, 862, L18 [6.1](#)
- Gu, M., Conroy, C., Diemer, B., et al. 2020, arXiv e-prints, arXiv:2010.04166 [6.1](#)
- Gunn, J. E., Carr, M., Rockosi, C., et al. 1998, *AJ*, 116, 3040 [2.3](#)
- Gwyn, S. D. J. 2014, in *Astronomical Society of the Pacific Conference Series*, Vol. 485, *Astronomical Data Analysis Software and Systems XXIII*, ed. N. Manset & P. Forshay, 387 [2.3](#)
- Jensen, J. B., Blakeslee, J. P., Ma, C.-P., et al. 2021, *ApJS*, 255, 21 [2.3](#)
- Johansson, J., Thomas, D., & Maraston, C. 2012, *MNRAS*, 421, 1908 [4.3](#)
- Kennicutt, R. C., & Evans, N. J. 2012, *Annual Review of Astronomy and Astrophysics*, 50, 531 [6.1](#)
- Kroupa, P. 2001, *Monthly Notices of the Royal Astronomical Society*, 322, 231 [1](#)
- Kroupa, P., Weidner, C., Pflamm-Altenburg, J., et al. 2013, *The Stellar and Sub-Stellar Initial Mass Function of Simple and Composite Populations*, ed. T. D. Oswalt & G. Gilmore, Vol. 5, 115 [1](#)
- Kurucz, R. 1993, *SYNTHES Spectrum Synthesis Programs and Line Data*. Kurucz CD-ROM No. 18. Cambridge, 18 [3.1](#)
- Kurucz, R. L. 1970, *SAO Special Report*, 309 [3.1](#)
- La Barbera, F., Ferreras, I., Vazdekis, A., et al. 2013, *MNRAS*, 433, 3017 [6.1](#)
- La Barbera, F., Vazdekis, A., Ferreras, I., et al. 2019, *MNRAS*, 489, 4090 [1, 6.1](#)
- Lasker, R., van den Bosch, R. C. E., van de Ven, G., et al. 2013, *MNRAS*, 434, L31 [1](#)
- Law, D. R., Chierinka, B., Yan, R., et al. 2016, *The Astronomical Journal*, 152, 83 [2.4](#)
- Li, H., Ge, J., Mao, S., et al. 2017, *ApJ*, 838, 77 [1, 6.1](#)
- Liepold, C. M., Quenneville, M. E., Ma, C.-P., et al. 2020, *ApJ*, 891, 4 [1](#)
- Ma, C.-P., Greene, J. E., McConnell, N., et al. 2014, *ApJ*, 795, 158 [2.1, 2.2, 2.3](#)
- Martín-Navarro, I., La Barbera, F., Vazdekis, A., et al. 2015, *MNRAS*, 451, 1081 [1, 6.1](#)
- Martín-Navarro, I., Pinna, F., Coccatto, L., et al. 2021, arXiv e-prints, arXiv:2107.14243 [1](#)
- McConnell, N. J., Ma, C.-P., Murphy, J. D., et al. 2012, *ApJ*, 756, 179 [1](#)
- McDermid, R. M., Cappellari, M., Alatalo, K., et al. 2014, *The Astrophysical Journal*, 792, L37 [6.1](#)
- Moustakas, J., Lang, D., Schlegel, D. J., et al. 2021, in *American Astronomical Society Meeting Abstracts*, Vol. 53, *American Astronomical Society Meeting Abstracts*, 527.04 [2.3, 4.1](#)
- Newman, A. B., Smith, R. J., Conroy, C., Villaume, A., & van Dokkum, P. 2017, *ApJ*, 845, 157 [1, 2.4, 3.1, 5, 4.2, 5, 9, 6.2](#)
- Oser, L., Ostriker, J. P., Naab, T., Johansson, P. H., & Burkert, A. 2010, *ApJ*, 725, 2312 [6.1](#)
- Parikh, T., Thomas, D., Maraston, C., et al. 2018, *MNRAS*, 477, 3954 [1, 6.1](#)
- Patel, S. G., van Dokkum, P. G., Franx, M., et al. 2013, *ApJ*, 766, 15 [6.1](#)
- Prochaska, J. X., Hennawi, J. F., Westfall, K. B., et al. 2020, *Journal of Open Source Software*, 5, 2308 [2.4](#)
- Prochaska, J. X., Hennawi, J., Cooke, R., et al. 2020, *pypeit/PypeIt: Release 1.0.0*, doi:10.5281/zenodo.3743493 [2.4](#)
- Rosani, G., Pasquali, A., La Barbera, F., Ferreras, I., & Vazdekis, A. 2018, *MNRAS*, 476, 5233 [4.6](#)
- Salpeter, E. E. 1955, *ApJ*, 121, 161 [3.1](#)
- Scalo, J. M. 1986, *Fund. Cosmic Phys.*, 11, 1 [1](#)
- Schwarzschild, M. 1979, *ApJ*, 232, 236 [1, 5](#)
- Sharda, P., & Krumholz, M. R. 2021, arXiv e-prints, arXiv:2107.08634 [6.1](#)
- Smith, R. J. 2014, *MNRAS*, 443, L69 [1, 4.5, 4.5, 5](#)
- . 2020, *ARA&A*, 58, 577 [1](#)
- Smith, R. J., Lucey, J. R., & Carter, D. 2012, *Monthly Notices of the Royal Astronomical Society*, 426, 2994 [1](#)
- Smith, R. J., Lucey, J. R., & Conroy, C. 2015, *MNRAS*, 449, 3441 [6.1](#)
- Spiniello, C., Barnabè, M., Koopmans, L. V. E., & Trager, S. C. 2015, *MNRAS*, 452, L21 [1](#)
- Spiniello, C., Koopmans, L. V. E., Trager, S. C., Czoske, O., & Treu, T. 2011, *MNRAS*, 417, 3000 [1, 6.1](#)
- Spiniello, C., Trager, S. C., Koopmans, L. V. E., & Chen, Y. P. 2012, *ApJ*, 753, L32 [1](#)
- Thomas, D., Maraston, C., & Bender, R. 2002, arXiv, 897 [4.2](#)
- Thomas, D., Maraston, C., Bender, R., & Mendes de Oliveira, C. 2005, *ApJ*, 621, 673 [4.3, 6.1](#)
- Thomas, D., Maraston, C., Schawinski, K., Sarzi, M., & Silk, J. 2010, *Monthly Notices of the Royal Astronomical Society* [4.3](#)
- Thomas, J., Ma, C.-P., McConnell, N. J., et al. 2016, *Nature*, 532, 340 [5](#)
- Thomas, J., Saglia, R. P., Bender, R., et al. 2011, *MNRAS*, 415, 545 [1](#)
- Trager, S. C., Faber, S. M., Worthey, G., & González, J. J. 2000, *The Astronomical Journal*, 120, 165 [4.3](#)
- Treu, T. 2010, *ARA&A*, 48, 87 [1, 5, 4.2, 6.1](#)
- Trujillo, I., Ferré-Mateu, A., Balcells, M., Vazdekis, A., & Sánchez-Blázquez, P. 2014, *ApJ*, 780, L20 [6.1](#)
- van Dokkum, P., Abraham, R., Romanowsky, A. J., et al. 2017, *ApJ*, 844, L11 [1, 3.2, 6.1](#)
- van Dokkum, P. G., Bloom, J., & Tewes, M. 2012, *L.A. Cosmic: Laplacian Cosmic Ray Identification*, ascl:1207.005 [1, 2.4](#)
- van Dokkum, P. G., Whitaker, K. E., Brammer, G., et al. 2010, *ApJ*, 709, 1018 [1, 6.1](#)
- Vazdekis, A., Koleva, M., Ricciardelli, E., Röck, B., & Falcón-Barroso, J. 2016, *MNRAS*, 463, 3409 [1](#)
- Veale, M., Ma, C.-P., Greene, J. E., et al. 2017a, *MNRAS*, 471, 1428 [2.1, 2.2](#)
- Veale, M., Ma, C.-P., Greene, J. E., et al. 2018, *Monthly Notices of the Royal Astronomical Society*, 473, 5446 [2.1, 2.3](#)
- Veale, M., Ma, C.-P., Thomas, J., et al. 2017b, *MNRAS*, 464, 356 [2.1, 4.1, 4.2, 4.6](#)
- Villaume, A., Conroy, C., Johnson, B., et al. 2017, *ASTROPHYS J SUPPL S*, 230, 23 [1, 3.1, 4.2, 6.1](#)
- Weilbacher, P. M., Palsa, R., Streicher, O., et al. 2020, *A&A*, 641, A28 [2.4](#)
- Wing, R. F., & Ford, W. Kent, J. 1969, *PASP*, 81, 527 [1](#)
- Wolf, J., Martinez, G. D., Bullock, J. S., et al. 2010, *Monthly Notices of the Royal Astronomical Society*, 406, 1220 [5](#)
- Worthey, G., & Collobert, M. 2003, *ApJ*, 586, 17 [4.3](#)
- Zhou, S., Mo, H. J., Li, C., et al. 2019, *MNRAS*, 485, 5256 [6.1](#)